

SIMULATIONS OF THE FEBRUARY 1979 STRATOSPHERIC SUDDEN WARMING:
MODEL COMPARISONS AND THREE-DIMENSIONAL EVOLUTION

G. L. Manney

Jet Propulsion Laboratory/California Institute of Technology,
Pasadena, CA 91109

J. D. Farrara and C. R. Mechoso

University of California, Los Angeles,
Los Angeles, CA 90024

Abstract

The evolution of the stratospheric flow during the major stratospheric sudden warming of February 1979 is studied using two primitive equation models of the stratosphere and mesosphere. One model uses log-pressure as a vertical coordinate (the SMM), the other uses potential temperature (the ECM). Both models produce successful simulations of the warming, capturing the splitting of the vortex. The simulated fields show small scale structures, such as narrow baroclinic zones and differential advection of Rossby-Ertel potential vorticity (PV). The ECM produces sharper temperature gradients, as well as a more realistic recombination and recovery of the polar vortex in the mid-stratosphere after the warming. It is suggested that this is due to the automatic increase in vertical resolution near such gradients, and better conservation properties for PV in this model.

A schematic description of the three-dimensional evolution of the polar vortex is presented. Strong upward velocities develop in the lower stratosphere on the west or cold side of a baroclinic zone as it forms over Europe and Asia. Strong downward velocities appear in the upper stratosphere on the east, or warm side, strengthening the temperature gradients. After the peak of the warming, vertical velocities decrease, downward velocities move into the lower stratosphere and upward velocities move into the upper stratosphere. The region of high temperatures in the upper stratosphere moves westward over the region of low temperatures in the lower stratosphere.

Air with high ozone mixing ratios is advected towards the pole from low latitudes during the warming, and air with low ozone mixing ratios is transported to the mid-stratosphere from both higher and lower altitudes along the baroclinic zone in the polar regions. Trajectories of particles moving around the vortex oscillate up and down as they move through regions of ascending and descending motions.

Comparison of SMM simulations with forecasts performed using the UCLA GCM

1. introduction

Stratospheric sudden warmings result in convoluted flows in the middle atmosphere, where many scales of vertical and horizontal motion are generated (Fairbridge et al. 1990, hereafter FFO). The dynamical processes involved in a major stratospheric sudden warming are particularly complex and intriguing. One such event, which has motivated several observational, theoretical, and modeling studies developed in middle to late February 1979 (see Andrews et al. 1987, chapter 6 for a review; also Mechoso et al. 1985 and Mechoso and Arakawa 1986). In this paper, we present a comprehensive picture of the three-dimensional evolution of the stratospheric flow during this warming. Our goal is to gain insight into model features that are important in successfully simulating such events.

Mechoso et al. (1985, hereafter M) and Mechoso and Arakawa (1986, hereafter MA) performed experimental forecasts of the February 1979 stratospheric sudden warming using a version of the UCLA general circulation model (GCM) with the top at 1 mb. M shows significant sensitivity of the stratospheric forecast to horizontal resolution, and suggests that this is a manifestation of sensitivity to errors in tropospheric forecasts. MA confirms this view by showing that low resolution forecasts of the warming can be dramatically improved by updating selected tropospheric fields with observed values during the prediction.

Although M and MA demonstrate that the GCM can predict stratospheric sudden warmings from several days in advance, the forecast fields are not ideal for detailed study of the stratosphere. The model top at 1 mb is too low for analysis of the upper stratosphere. In addition, the GCM has only six levels between 100 mb and its top at 1 mb, giving a vertical resolution of approximately 6 km. FFO show, in simulations using a primitive-equation model of the stratosphere and mesosphere (including one of the Febru-

stratosphere than the GCM, we can significantly improve the simulation of these small-scale features of the stratospheric warming and explore their structure and interactions with the large scale flow. To investigate these issues, we use the UKMO Stratosphere-Mesosphere Model (SMM) to simulate the February 1979 major warming. The horizontal resolution of this model is comparable to the GCM, but it has higher vertical resolution.

Another approach which has important advantages in modeling the atmosphere is to use entropy as the vertical coordinate (Arakawa et al. 1992). Since isentropic surfaces are material surfaces under adiabatic conditions, the vertical resolution of the model automatically increases in regions of strong temperature gradients. In addition, using an isentropic coordinate, the Rossby-Ertel potential vorticity can be simply expressed, making it easy to conserve in a discrete system. One can also obtain a quasi-Lagrangian view of atmospheric motions. A spectral, entropy coordinate model (ECM) of the stratosphere and mesosphere was recently developed at UCLA and the United Kingdom Meteorological Office (UKMO; Mike Fisher, private communication). The ECM incorporates a tracer transport algorithm, with transport of ozone interactive with the radiation code.; it also includes an on-line trajectory calculation. We use this model to simulate the February 1979 stratospheric sudden warming, and results are compared to those from the SMM.

In the following, we first describe and compare simulations performed with the two stratospheric models. We use the results of these simulations, including tracer transport and trajectory calculations, to examine the three-dimensional evolution of the flow during this major warming and subsequent recovery. Finally, simulations with the SMM are compared with the GCM forecasts described by M and MA.

2. The Data and Models

a. Data and Observed Evolution of the Flow

Two sets of observational data are used to initialize the models and verify results. National Meteorological Center (NMC) temperatures and geopotential heights are provided on 65 by 65 polar stereographic grids for each hemisphere at 18 pressure levels from 1000 to 0.4 mb. Above 100 mb, the NMC geopotential height fields are produced by using retrievals from stratospheric sounding units on board satellites and the 100 mb analyses. Details of the data retrieval scheme are given by Gelman et al. (1986) and references therein. The levels in the stratosphere are 100, 70, 50, 30, 10, 5, 2, 1, and 0.4 mb. The latter level is well above the weighting function peak of the highest satellite channel used, and is therefore unreliable; 0.4 mb data are not used in this study.

LIMS temperatures, geopotential heights, and ozone mixing ratios are provided in the form of Fourier coefficients for the zonal mean and first six zonal harmonics at 4 degree latitude intervals from 64 S to 84 N, as described by Leovy et al. (1985). They are given at 18 pressure levels between 1000 and 0.05 mb, corresponding to a vertical resolution of approximately 3 km. Data at 0.05 mb were not used due to the large number of missing values. LIMS data are used for verification of model results, since fields such as winds calculated from them are somewhat less noisy than from NMC data, and their vertical resolution is more comparable to that of the stratospheric models. LIMS data are not used for boundary fields, since their lowest level is 100 mb.

The major stratospheric warming that developed in February 1979 has been analyzed in a number of studies (Andrews et al, 1987 and references therein). We briefly describe the evolution of the flow as a context for our model comparisons. Figure 1 shows 10 mb geopotential heights and temperatures from LIMS data for selected days

Aleutian high centered near 180° . By 19 February, a second anticyclone can be seen forming near 0° . By 23 February, the two anticyclones have merged across the pole, and the cyclonic polar vortex is split into two well separated vortices, one over North America (the "North American" vortex), and the other over northern Europe and Russia (the "Eurasian" vortex). The Eurasian vortex is slightly stronger than the North American vortex. The anticyclone remains over the pole through 1 March, after which the two cyclonic vortices recombine (with the North American vortex becoming much weaker) to form a single vortex much reduced in size from its pre-warming dimensions. This vortex, and a weakened Aleutian high move slowly westward, with the vortex positioned over eastern North America on 13 March.

During 19 through 21 February, temperatures increase west of the Aleutian high, with the most dramatic increase between 23 and 25 February; during this time, strong, horizontal temperature gradients are seen toward the eastern side of the Eurasian vortex. Figure 2 shows a longitude height cross-section of temperature at 60°N from LIMS data on 25 February in which strong vertical temperature gradients (approximately 6 K/km) are also apparent. The horizontal resolution of both LIMS and NMC data is about 20 degrees in longitude (Clough et al. 1985, Leovy et al. 1985); this coarse horizontal resolution tends to smooth the temperature gradients in observations (FIO). FIO showed vertical temperature profiles reported by radiosondes with similar strong temperature gradients. These regions of strong temperature gradients are referred to as baroclinic zones in this study.

Geopotential heights and temperatures at 10 mb from NMC analyses provide a similar picture; during the peak of the warming, the separation of the two cyclonic vortices is slightly less, and the North American vortex is slightly stronger. Since the effective vertical resolution of the NMC data is near 12 km (Clough et al, 1985), the baroclinic zone is even less well resolved, but interpolated fields still suggest vertical temperature gradients

where ζ_θ is the vertical component of the relative vorticity computed on θ surfaces, $f = 2\Omega \sin(\text{latitude})$, g is acceleration due to gravity, and $\theta = T(p_0/p)^{\kappa}$ is potential temperature. For adiabatic, inviscid flow, Q is conserved along a parcel trajectory, so contours of Q on isentropic surfaces can be used to approximately follow the motion of air (Hoskins et al. 1985; Clough 1985; ITO). Q was calculated from LIMS data, using an algorithm similar to that described by Newman et al. (1989). These fields, although somewhat noisy, give a picture of the large scale evolution, Figure 3 shows Q for 21 February (near the beginning of the warming), 25 Feb, 27 Feb, 1 Mar, 3 Mar (near and after the peak of the warming, and 11 March (after the two cyclonic vortices have recombined). These distributions will be compared with results of SMM and ECM simulations.

b. The Models

The Stratosphere-Mesosphere Model (SMM) is based on the primitive equations with horizontal velocity and temperature as prognostic variables. A log-pressure vertical coordinate is used. In the horizontal, the equations are discretized to fourth-order accuracy on an 'A' grid (Arakawa and Lamb 1977). The SMM incorporates the radiation calculation of Shine (1987). The ozone distribution is prescribed, zonally symmetric, and corresponds to an observed climatology (Klenk et al. 1983). A linear relaxation of the wind field to zero (Holton 1976) is included to represent the effect of sub-grid scale processes, including gravity wave breaking. Further details of the SMM are given by Fisher (1987).

The lower boundary of the SMM is at 100 mb and the top at 0.01 mb. There are 32 levels in the vertical, resulting in a vertical resolution of about 2 km. The horizontal resolution is 5° longitude by 5° latitude. The geopotential height one grid space below the first model level is prescribed as a daily sequence of observed fields that are linearly

The use of entropy or potential temperature as the vertical coordinate in atmospheric models has several advantages (Arakawa et al. 1992). Coordinate surfaces are material surfaces for adiabatic processes. Ertel's potential vorticity (PV) can be simply expressed, making it easy to conserve in a discrete system. In addition, one can obtain a quasi-Lagrangian view of atmospheric motions.

The Entropy Coordinate Model (ECM) is a spectral, isentropic coordinate version of the SMM, developed recently by Mike Fisher (paper in preparation) at UCLA and the UK MO. The vertical coordinate is $s = C_p \ln(\theta/\theta_0)$. The model prognostic variables are velocity streamfunction, velocity potential, and pseudo-density (dp/ds). Two terms are included to represent the effect of sub-grid scale processes, an iterated Laplacian and a simple linear drag as used in the SMM.

The ECM also uses the radiation scheme of Shine (1987). In one version of the model, ozone is a three-dimensional, prognostic field, and is fully interactive with the radiation parameterization. Photochemistry is crudely parameterized as a relaxation of ozone mixing ratio towards the climatological fields. The model can also be run using a prescribed, climatological distribution of ozone in the radiation calculation, as in the SMM. Since a detailed description of the ECM has not been published, the major features of the model are described in the Appendix.

For most of the simulations, the lower boundary of the ECM is at 400° K (near 100 In b), and the upper boundary at 4000 K (near .03 mb), with 15 levels in the vertical, equally spaced in s . This gives better resolution in the stratosphere than the mesosphere, with the vertical resolution in the mid stratosphere typically being about 3 km away from strong temperature gradients. A triangular truncation at wavenumber 30 (T30) is used for most of the simulations described here, resulting in a horizontal resolution similar to the SMM. The Montgomery streamfunction is specified at the lower boundary.

The version of the GCM used for experimental forecasts of the February 1979

were performed from initial conditions corresponding to 15 February 1979 and 17 February 1979 at two horizontal resolutions, 4° latitude by 5° longitude, and 2.4° latitude by 3° longitude. initialization was done using a combination of FGGE Level 11 analyses and National Meteorological Center (NMC) height and temperature fields, as described by M. We concentrate on the higher resolution forecasts, which were more successful than those with low resolution.

Several datasets have been used for initialization and boundary fields in our simulations. NMC data were used for initial and boundary fields for SMM and ECM runs from 15 and 17 February, and these two sets of simulations are directly compared. In these ECM simulations, the ozone field is initialized from the climatology described above. Additional ECM simulations were done from 17 February with LIMS data (Leovy et al. 1985) used for initialization. In some of these cases, LIMS ozone is used in the initialization.

SMM runs starting on 15 and 17 February have also been done with the same initial fields used by M and MA for the GCM, and with the lower boundary given by the 100 mb heights from the high resolution (2.4° by 3°) GCM forecasts. These 141111S are most directly comparable to the GCM forecasts. SMM runs have also been done using the FGGE data that were used to initialize the GCM for boundary and initial fields.

Most SMM and ECM simulations are ten days long, as are the GCM forecasts. A simulation from 17 February 1979 with each of the stratospheric models is extended through 13 March, so that the recovery of the vortex after the warming can be examined. For the SMM, the simulation using NMC data for initialization was extended; for the ECM, the simulation initialized with LIMS data (and LIMS ozone) and a simulation using NMC data are extended. Table 1 shows the studies that will be used for intercomparison between different models. Table 2 shows additional ECM simulations that were done to examine the sensitivity of that model to various factors.

3. Stratospheric Model Comparisons

a. SMM and ECM comparisons

Both SMM and ECM simulations from 15 February and 17 February were performed using NMC data to provide initial and boundary fields. ECM simulations have been done with the same prescribed time-dependent ozone distributions used in the SMM, and with advection of ozone. A comparison of the results of these simulations shows that the dynamical fields are nearly identical. Simulations with a prescribed ozone distribution will be compared directly to SMM fields. In general, both stratospheric models succeed in producing an evolution characterized by a vortex split and a major wave 2 type warming. We examine here similarities and differences between the simulations with each model. It is immediately clear that the date of initialization is much less significant in the stratospheric models than in the GCM forecasts; simulations from 15 February in the ECM and SMM are only slightly less successful than those from 17 February. Therefore, after briefly describing the simulations from 15 February, we concentrate on simulations started from 17 February.

At 10 mb, in simulations started from 15 February, the region of low temperatures associated with the Eurasian vortex is larger and colder than observations, and that associated with the North American vortex somewhat warmer. In the ECM simulation, the North American vortex is slightly weaker than observations and the Eurasian vortex somewhat stronger. In contrast, in the Sh4M simulation, the strength of the two vortices is more equal, with the Eurasian vortex weaker than observations. On 25 Feb (Fig. 1c), there is a region of high temperatures near 90°E and 50° latitude, with a maximum value near 260 K. Neither simulation has temperatures above 245 K at this level on this day, and in both the region of high temperatures is closer to the pole. The SMM simulation

higher altitudes.

Figure 4 shows geopotential heights and temperatures from SMM and ECM simulations from 17 February on 21 and 25 February. The SMM simulation is somewhat closer to observations than that from 15 February; the ECM simulation is very similar to that from 15 February. Figure 4 shows that the North American vortex at 10 mb is slightly too strong in the SMM simulation, and slightly too weak in the ECM simulation. On 25 February, the region of high temperatures is closer to the pole and not as warm as observations. Figure 5 shows longitude/height cross-sections of temperature from these runs for 23 February. Again, in both cases, the strongest vertical temperature gradients are near 5 K/km.

Rossby-Ertel potential vorticity on 21, 23 and 25 February in the simulations from 17 February is shown in Fig. 6. In both simulations low values of PV are being advected from low latitudes into the polar region east of the Eurasian vortex, and into the Aleutian anticyclone; similar advection can also be seen around the eastern edge of the North American vortex, especially in the SMM simulation. The SMM results show some regions of higher PV near the pole and the Aleutian anticyclone, especially on 23 February, possibly an artifact of polar filtering in the model (FFO).

In general, the results from the two models are quite similar, although the ECM nominally has coarser vertical resolution than the SMM. The isentropes shown in Fig. 5 reveal that the vertical resolution of the ECM near the baroclinic zone is near 2 km, similar to that of the SMM.

A number of additional simulations have been done using the ECM. One that is of particular interest was done from 17 February using LIMS data for initialization of the dynamical fields and the ozone distribution. The full version of the model with ozone transport interactive with the radiation scheme is used. The boundary fields used are the same as described above since LIMS data do not extend below 100 mb. Besides having

Figure 7 shows geopotential heights and temperatures at 10 mb from this simulation on 21 and 25 February. As in the other ECM simulations, the North American vortex is slightly weaker than observations and the Eurasian vortex slightly stronger. Also, although the high temperatures at 10 mb are near the values in observations, the region of warm temperatures does not come as far off the pole as in observations. Figure 8 shows a longitude/height cross-section of temperature on 23 February. Both horizontal and vertical temperature gradients are stronger here than in the simulations previously discussed, with vertical temperature gradients reaching about 9 K/km. Maximum temperatures are higher than observations by as much as 10 K, and are centered at slightly lower altitude. Figure 9 shows PV fields for this simulation. A large region of low PV values is advected across the pole, consistent with PV maps calculated from observations, and with conservation of PV (FFO).

Vertical velocities were calculated from the SMM and ECM simulations, using the continuity equation and assuming that the divergence is zero at the top of the SMM, or at a pressure level near the top of the ECM (ECM results were interpolated to pressure surfaces for this calculation). FFO showed that substantial vertical velocities are associated with strong baroclinic zones. Figure 10 shows longitude/height cross-sections at 60°N and horizontal sections at 12.2 mb of vertical velocity on 23 February for the SMM run from 17 February using NMC data, the ECM run using NMC data, and the ECM run using LIMS data. The pattern is qualitatively similar in each case, although details vary considerably. Each shows a region of downward velocities throughout the stratosphere along the baroclinic zone, toward the warm, or eastward side. There is also a region of upward velocities farther east of the baroclinic zone in the upper stratosphere. Downward velocities in the mid-stratosphere are strongest in the SMM simulation. Both simulations initialized with NMC data also show very strong downward velocities in the lower mesosphere and upper stratosphere; this may be due to adjustment in the model from the ini-

... .. <

upward and downward velocities with upward velocities poleward of and west of the baroclinic zone, in the cold region, and downward velocities equatorward and east of the baroclinic zone, in the warm region. A weaker such dipole pattern appears at the location of the North American vortex, but has little tilt with height, and upward velocities lie directly west of downward velocities.

Since the recovery of the circulation after the warming depends more on processes taking place within the stratosphere rather than at tropopause level, and because the ECM should conserve PV better than the SMM, we expect greater differences in model performance during the recovery. Figure 11 shows 10 mb geopotential heights and temperatures, and 850 K PV on 5 and 11 March from SMM and ECM simulations started on 17 February using NMC data for initialization and boundary fields. On both days, the strength and position of the cyclonic vortex shown in the height fields are considerably closer to observations in the ECM than the SMM. While the cyclone is slightly stronger in the ECM simulation than in observations, both cyclone and anticyclone are much weaker in the SMM simulation, and on 5 March, two separate cyclonic vortices are still apparent. In the PV fields, the lack of conservation of PV in the SMM is obvious. In comparing model PV fields with those calculated from observations, one should consider that there may be apparent non-conservation of PV as a result of poor resolution in the data, rather than of any diabatic effects. The maximum PV values in the SMM simulation on 11 March are approximately half those on 25 February at the peak of the warming. The corresponding PV values in the ECM simulation decrease by approximately 20%. Maximum values calculated from LIMS data (Fig. 2) also decrease by approximately 20-30% during this time. The recovery of the vortex is considerably faster than would be expected from radiative cooling in the mid-stratosphere, where radiative time scales are 2-3 weeks (Dickinson 1973).

The ECM simulation using LIMS data for initialization was also extended through

b. *ECM Resolution and Boundary/Initialization tests.*

A number of additional ten-day runs were done using the ECM to assess the model sensitivity to details of the boundary and initial fields. These are summarized in Table 2.

We note the following points:

- There is little difference between runs where ozone is transported and interacts with the radiation calculation, and runs where the radiation calculation used a prescribed, time-dependent distribution of ozone corresponding to an observed climatology. Also, using climatological versus LIMS ozone for initialization when ozone is transported by the model does not produce large differences in the dynamical fields. This is consistent with the hypothesis that diabatic effects are not crucial for short (around 10 day long) simulations.
- Since the pressure at 400 K in the Northern Hemisphere during February is generally higher than 100 mb (near 150 mb around the Aleutian high), runs were done with the lower boundary at 420 K. The results do not show any significant differences from the simulations with the lower boundary at 400 K.
- Using 20 levels rather than 15 produced a slight improvement in the intensity of the North American Vortex.

The ECM becomes very demanding of computer resources as the model resolution is increased, mainly due to increases in resources required by the radiation code and ozone advection. To examine the sensitivity to model resolution, a modified version of the ECM was used in which the radiation code was replaced with a simple Newtonian cooling, as described by O'Neill and Pope (1988), and the tracer advection was removed; this model version is referred to as the "Mini-ECM". Over a short run, the removal of the radiation code should not have a very large effect. Mini-ECM runs were initialized with LIMS data. One run was made with the same resolution as the full ECM (T30 truncation,

Geopotential heights and temperatures at 10 mb for 21 and 25 February from the T60 and T30 runs are shown in Fig. 12. The T30 run shows similar failings to the corresponding ECM simulations: the North American vortex is too weak, and the anticyclone is too strong and too wide across the pole. Both deficiencies are alleviated to some extent in the T60 run. Since all the ECM simulations, which have poorer vertical resolution over most of their domain than the SMM, but similar horizontal resolution, tend to make the North American vortex too weak, we speculate that vertical resolution may be an important factor in reproducing the North American vortex. The T60 run also comes closer to reproducing the region of low temperatures over North America, which is not well represented in the T30 run, or in other simulations.

Maximum vertical temperature gradients in the T30 Mini-ECM run are about 10 K/km on 23 February (as opposed to about 9 K/km in the ECM simulation described earlier initialized with LIMS data). In the T60 run, maximum temperature gradients are about 9 K/km, also on the 23rd. As shown in Figure 13, on 25 February, the T60 run shows stronger temperature gradients associated with the North American vortex than with the lower resolution. We note that the North American vortex is less tilted than the Eurasian vortex, and thus the strong temperature gradients are mainly horizontal. Given the poor horizontal resolution of the data available, we cannot say whether this feature was present in the atmosphere. As in FFO, our results emphasize the importance of observation systems capable of higher horizontal and vertical resolutions that are currently available to improving our understanding of stratospheric dynamics.

4. Three-dimensional structure of the flow and transport during the warming

Each of the two stratospheric models (SMM and ECM) has produced successful simulations of the February 1979 sudden warming from several days in advance. We use

a. Three-dimensional structure and evolution of the flow

The three-dimensional structure of the flow is examined by inspection of an isosurface of PV on isentropic surfaces, throughout the warming, calculated from an ECM simulation started on 17 February. Fig. 14 shows an isosurface of PV where the values are scaled by a standard atmosphere value of $\partial\theta/\partial p$ (Baldwin and Holton 1988, Baldwin and Dunkerton 1989), so that PV has units of vorticity, and the range of values is similar at each level. The value selected represents a contour within the region of strong PV gradients, and as such is an approximate definition of the edge of the vortex. Also shown in Fig. 14 is the full PV field at 874 K, in the middle of the vertical range. As the warming develops and the polar vortex splits, we note the development of a strong westward tilt with height of the Eurasian vortex, and a similar but much weaker tilt in the North American vortex. The development of this tilt indicates that PV is being advected at different rates on different isentropic surfaces; this differential advection of PV contributes to the development of small vertical scale structure (FFO).

FFO analyzed a baroclinic zone obtained during a simulation of another stratospheric warming, at a time near the peak of the warming. This analysis showed that a thermodynamically indirect secondary circulation arose, mainly from adiabatic warming due to strong sinking motion on the warm (east) side of the baroclinic zone; the ageostrophic flow provided a feedback on the frontogenetic effect of the large-scale geostrophic flow, acting to strengthen the baroclinic zone. Here we show the time evolution of the baroclinic zone associated with the Eurasian vortex in a series of temperature and vertical velocity cross-sections from the ECM simulation that used JIM S data for initialization (Figure 15). As the baroclinic zone is forming, the strongest downward motion is in the upper stratosphere where the temperatures are high, and strong upward velocities appear in the lower stratosphere, to the west of the baroclinic zone, moving cold tempera-

region of downward velocities moves down and that of upward velocities up, and the strength of the vertical velocities diminishes, so that the vertical motion no longer strengthens the baroclinic zone. During this entire time period, the region of lowest temperatures in the lower stratosphere remains relatively stationary, while the region of highest temperatures moves westward and downward over it. The baroclinic zone itself also moves downward, and at the end of the episode, horizontal temperature gradients decrease, so that by 27 February, the strong gradients at 60° N are nearly vertical.

Figure 16 shows horizontal plots at 12.2 mb of vertical velocities and temperatures. There is a dipole type pattern of upward and downward velocities, with contours approximately orthogonal to those of the temperature field and downward velocities located on the eastward and equatorward side of the vortex, upward velocities on the westward and poleward side. Divergence is associated with the upward velocities and convergence with downward velocities.

Figure 17 shows a schematic of the vortex structure during the peak of the warming. Westward and poleward of, and below the baroclinic zone are divergence and upward motion in the cold region; eastward and equatorward of, and above the baroclinic zone, convergence and downward motion take place in the warm region. These "tilting" effects tend to increase the baroclinicity locally. After the baroclinic zone forms, the centers of upward (downward) velocities move above (below) the baroclinic zone, decreasing these effects. A qualitatively similar structure is seen when baroclinic zones develop in simulations of final warmings in both Northern and Southern Hemispheres (Manney et al., 1992).

b. Trajectory calculations

The trajectories of fluid parcels were estimated using the simulated velocity field

used near the poles. The trajectory time-step was 30 minutes. We present results obtained in simulations from 17 February.

Figure 18 shows several trajectories started at 30° N on 17 February at 850 K in the ECM from the simulation initialized using LIMS data. Parcels are advected across the pole, and around the Aleutian High. Those parcels that remain at low latitudes show little vertical motion. However, strong downward motion develops as parcels are advected around the equatorward and eastern side of the Eurasian vortex, consistent with the position of the strongest downward velocities (Fig. 18b). This is followed by strong upward motion as the particles are advected through the region of upward velocities on the westward and poleward side of that vortex.

Figure 19 shows trajectories started at 70° N also at 850 K. Parcels that start well within the vortex are confined to one of the vortices that develop during the warming, and circulate rapidly around that vortex. Vertical velocities vary as the parcels move through regions of upward and downward velocities as they circulate around a vortex. Parcels that start near the edge of the initial vortex either move away from the vortex or circulate within it, depending on the exact starting position. There are also parcels that start well outside the initial vortex and end up circulating around one of the vortices after they have split (not shown). As before, those parcels that move away from the vortex have small displacements in the vertical.

Qualitatively similar motions are also seen for particles started at higher (1100 K) and lower (600 K) levels. The general trend over the oscillatory vertical motion is for parcels to move down in the polar regions (Fig. 19b), as is expected during the winter season. There is also downward motion in the polar regions at lower and higher levels. Over the 10 day period shown, parcels started at 840 K and 70°N experience diabatic descent of as much as 6 Kd^{-1} ; parcels started at 600 K and 70°N experience diabatic descent up to 2.5 Kd^{-1} , and parcels started at 1100 K and 70°N experience diabatic

c. Transport of ozone in ECM simulations

Another way of examining the evolution of the flow is by looking at the motion of tracers. Ozone is of particular interest, due to concerns about anthropogenic influences on its distribution, and for comparison with the Southern Hemisphere where the ozone hole forms. Since ozone data are available from LIMS, the model can be initialized with a synoptic, three-dimensional ozone field. Figures 20 and 21 show horizontal and vertical sections, respectively, of ozone during the simulation with the ECM initialized with LIMS data. Plots of ozone from LIMS data are shown for comparison. Since photochemistry is very crudely represented by a relaxation to climatology, ozone in fact behaves very much like a passive tracer. The horizontal fields of ozone thus strongly resemble those of PV.

Initially, there are low ozone mixing ratios in the polar vortex, as well as in the Aleutian high and the developing high over Northern Europe. As the vortex splits, high ozone values are advected across the pole from low latitudes, forming strong horizontal gradients as the region of low ozone associated with the Aleutian high is also displaced toward the polar regions. Since the distribution of ozone in the mid-stratosphere is controlled mainly by dynamical processes, it is not surprising that the ECM does well in reproducing the observed field of ozone at this level.

From the vertical cross-sections, we see that high ozone is advected into a region in the mid-stratosphere to the east of the Eurasian vortex and the baroclinic zone; a smaller concentration of high values is also seen to the east of the North American vortex. High ozone values are advected mainly from lower latitudes around the eastern side of each vortex, while low ozone values are transported from both higher and lower altitudes along the baroclinic zone. Again, the main features of the observed ozone distribution are obtained in the simulation.

S. Comparison of SMM simulations and GCM forecasts

M and MA performed experimental forecasts of the February 1979 stratospheric sudden warming using the UCLA GCM, with a resolution of 2.4° latitude by 3° longitude. Unlike the stratospheric models, these forecasts were highly sensitive to the starting date. The forecasts started from 15 February did not produce the major warming and the splitting of the vortex, while those from 17 February were successful in this regard. Lower resolution simulations (4° latitude by 5° longitude) were less successful from either starting day. M suggested that these results were due primarily to the effect of errors in the tropospheric forecast.

To further explore this hypothesis, we performed SMM simulations using the same data that was used to initialize the GCM for boundary and initial fields. In addition, another set of SMM simulations uses boundary fields defined by the 100 mb geopotential heights from the higher resolution GCM forecasts. In this second set of simulations, the SMM performance will be affected by any errors present in the tropospheric forecast that affected the stratospheric forecast in the GCM. Although the horizontal grid spacing in the SMM is approximately twice that in the high resolution GCM, the vertical grid spacing is about one-third that of the GCM, and the SMM model top is much higher.

Figure 22 shows SMM geopotential heights for a simulation from 15 February, where FGGF data are used for initialization and boundary fields. This simulation reproduces the observed splitting of the vortex, although both cyclonic vortices are too weak (especially the North American vortex) and too far from the pole; the anticyclone is much wider over the pole than in observations. In contrast, both the GCM forecast from 15 February (Figure ? in M), and the SMM simulation with GCM fields used at the lower boundary (not shown), show a tendency towards splitting of the vortex on 21 February, but the vortex does not completely split as is apparent in the results corresponding to 25

These results support the hypothesis that errors in the tropospheric forecast are largely responsible for the failure of the GCM forecast from 15 February. MA showed that in predicting the split of the polar vortex the success of the forecast from 15 February is dramatically improved by updating selected fields in the troposphere using FGGE data. This SMM simulation provides further evidence that the stratospheric forecast is very sensitive to errors in the tropospheric forecast.

Figure 23 shows 10 mb geopotential heights from SMM simulations and high resolution GCM forecasts initialized on 17 February. The two SMM simulations use FGGE data and 100 mb GCM fields, respectively, for their boundary fields. The SMM simulation using GCM boundary fields reproduces most of the deficiencies of the GCM forecast: the anticyclone is too far off the pole, the Eurasian vortex is too strong throughout, and both vortices are too close to the pole. In the SMM simulation using GCM boundary fields, the North American vortex is also too strong. In the SMM simulation using FGGE data, the anticyclone is too wide over the pole, and the North American vortex is too weak. The strength of the Eurasian vortex is near that of observations in this case.

In general, the SMM using the 100 mb GCM fields for boundary conditions produces horizontal fields very similar to those in the GCM. Figure 24 shows a longitude/height cross-section of temperatures at 60 N, from the GCM and the two SMM simulations from 17 February. Horizontal temperature gradients are similar in the GCM and SMM with GCM boundary, but vertical temperature gradients in the SMM simulation are approximately twice as strong as those in the GCM forecast (6 K/km vs. 3 K/km). The effect of improved vertical resolution in the stratosphere is thus apparent. In this case, the lower horizontal resolution of the SMM does not appear to materially affect the simulation. In the SMM simulation with FGGE data, both vertical and horizontal temperature gradients are slightly stronger than those in the SMM simulation with GCM fields.

5. Discussion and conclusions

Two primitive equation models of the stratosphere and mesosphere with nearly the same parameterizations of physical processes, but different vertical coordinates are used to simulate the stratospheric sudden warming of February 1979. One model uses pressure as a vertical coordinate (the SMM), the other uses potential temperature (the ECM). Both models produce successful simulations of the warming that show many of the small-scale features that are known to develop during such events (FFO) in more detail than can be provided by current observational data. Most results from these simulations show relatively subtle differences between the two models. From slight differences in the shape and positions of the polar vortices, it is not possible to say that either model is clearly superior, particularly given the inadequate resolution of the data to which model results can be compared.

The ECM nominally has lower vertical resolution than the SMM. One of the advantages of the entropy vertical coordinate is that as small scale structure such as a baroclinic zone develops, the isentropes are tilted and packed together; since the flow is approximately along isentropes, this implies that the vertical resolution is automatically increased without the need to increase the number of model levels. Comparison of SMM simulations with UCLA GCM forecasts, and resolution tests with the ECM shows the importance of vertical resolution in simulating events such as stratospheric warmings where small scale structure develops within the large-scale flow.

In simulations of the recovery of the polar vortex after the warming, the ECM performed significantly better than the SMM in the mid-stratosphere. As described by FFO, during the warming, high PV values are drawn out into narrow tongues, which eventually are lost due to resolution and truncation effects in the model. Since the recombination of centers of high PV is necessary to the recovery of the vortex, and since this recovery

motions. The use of entropy as the vertical coordinate simplifies the expression of PV, making it easy to conserve in a vertically discrete system. The success of the ECM in simulating the recovery of the flow after a major warming appears to be an advantage of using entropy as a vertical coordinate.

A comparison of runs with varying resolutions using a simplified version of the ECM suggests that further improvement of the results could be gained by increasing both horizontal and vertical resolution. With the advent of more powerful computers, this should become feasible for both spectral and finite-difference models.

We examine the simulated three-dimensional structure and evolution of the polar vortex during the warming. During the warming, and formation of a narrow baroclinic zone associated with the Eurasian vortex, the Eurasian vortex tilts strongly westward with height throughout the stratosphere. This shows the differential advection of PV noted by FFO, where high PV values are advected at different rates on different isentropic surfaces. The differential advection of PV increases the importance of adequate vertical resolution, since the effective vertical scale of high PV features is thereby reduced (FFO).

A schematic description of the evolution of a baroclinic zone and its relation to the polar vortex is presented. Strong vertical velocities develop in a dipole pattern along the eastern side of the vortex as the baroclinic zone forms. Upward velocities are in the lower stratosphere, on the westward and poleward side of the baroclinic zone, in the region of low temperatures; downward velocities are on the eastward and equatorward side, in the region of high temperatures. This pattern advects high temperatures downward to the east and low temperatures upward to the west, increasing the strength of the baroclinic zone. After the time of strongest temperature gradients, the downward velocities move into the lower stratosphere and the upward velocities move up. The strength of the vertical velocities decreases. The region of high temperatures in the upper stratosphere moves westward over the region of low temperatures in the lower stratosphere.

baroclinic zone.. Additional details of transport are elucidated by trajectory calculations. Trajectories of particles caught in the Eurasian vortex after the vortex splits show oscillatory upward and downward motion as they move through the regions of upward and downward velocities. The overall tendency is for particles to move downward in the polar regions.

Comparison of SMM simulations with forecasts using the UCLA GCM reinforces the importance of vertical resolution in the stratosphere in modeling the stratosphere; an otherwise successful GCM forecast did not reproduce the baroclinic zone associated with the Eurasian vortex, while an SMM simulation using the GCM prediction for 100 mb for boundary fields did. The comparison of GCM and SMM results also confirms the sensitivity of stratospheric forecasts to tropospheric forecasts suggested by M and MA; SMM simulations using GCM fields for the lower boundary reproduced most of the same failings as the GCM forecasts.

The three-dimensional picture presented of the evolution of the flow during a stratospheric sudden warming shows the development of prominent features in a broad range of spatial scales. This emphasizes the importance of adequate resolution, especially vertical resolution, whether in model simulations or in data, in resolving these features for better understanding the dynamics and structure of the stratospheric polar vortex.

Acknowledgments. Special thanks to Mike Fisher for his assistance and advice in using the entropy coordinate model. Paul Newman provided original software that was adapted to calculate PV from data. The research at JPL was carried out by the Jet Propulsion laboratory/California institute of Technology, under a contract with the National Aeronautics and Space Administration (NASA). Computational support was provided by the JPL Supercomputing Project, which is sponsored by JPL and the NASA Office of Space Science and Applications. 3-d graphics were produced by Erik Mattson of the JPL

Appendix: Entropy Coordinate Model Description

The entropy coordinate model is based on the primitive equations expressed in terms of a vertical coordinate $s = C_p \log(\theta/\theta_0)$. Model levels are equally spaced in s giving slightly higher resolution in the stratosphere than the mesosphere. The reference potential temperature, θ_0 , may be set arbitrarily, and a value of 1 K is used here. The model is divided into discrete layers in the vertical, with the prognostic variables (velocity streamfunction, ψ , velocity potential, χ , and pseudo-density, $m = dp/ds$) defined at the center of each level. The hydrostatic equation is discretized using the energy conserving formulation of Hsu and Arakawa (1990).

The Montgomery streamfunction is specified at the isentropic surface which is the lower boundary of the model as a sequence of fields which are linearly interpolated in time. The center of the lowest layer for which the prognostic variables are held is one vertical grid-spacing above the lower boundary level. The upper boundary condition is provided by assuming that the temperature at the upper boundary of the top layer of the model is identical to that at the lower boundary of that layer. Use of this upper boundary condition has been found to reduce the amplitude of oscillations in m near the top of the model (Mike Fisher, private communication).

A semi-implicit method is used to integrate the prognostic equations in time. The non-linearity of the hydrostatic equation with respect to pressure requires that the pressure gradient be split into two terms, one of which is linearly related to pressure, and is integrated implicitly, and a remainder which is integrated with a leapfrog timestep. A mild time filter (Asselin, 1972) is applied to the prognostic fields, ozone pseudo-density and any other trace species in the model, to prevent the growth of computational modes.

The nonlinear terms in the discrete-time prognostic equations are calculated using the spectral transform method (Orszag 1970, Eliassen et al, 1972), where the prognostic

that quadratic terms are evaluated without aliasing.

Longwave and shortwave radiation are parametrized using the scheme of Shine (1987). The shortwave parametrization is based on that of Strobej (1978). The longwave scheme uses the Curtis matrix method to parameterize emission and absorption of longwave radiation in the 9.6μ ozone and 15μ carbon dioxide bands. A simple parametrization of the radiative effects of water vapor is also included. The radiation parametrization was adapted from the version used in the isobaric model (SMM). For the shortwave and water vapor schemes, this requires only that the schemes account for the fact that pressure varies in the horizontal. The longwave ozone parametrization was adapted by calculating a Curtis matrix for each vertical column at each radiative time step (3 hours for the runs discussed here). The carbon dioxide parametrization is left unaltered from that used in the isobaric version of the model, and temperatures and heating rates are linearly interpolated between the pressure grid required by the longwave parametrization and the entropy grid used by the model,

The "vertical velocity", \dot{s} , is given by $\dot{s} = H/T$, where H is the heating rate and T is temperature. Time integration of vertical advection terms is carried out using a first order, forward scheme. This scheme is usually unstable for advection equations, but has proved stable in practice,

The effect of gravity waves on the mesospheric flow is represented crudely by a simple linear drag, following Holton (1976), with the drag coefficient increasing linearly with height in the mesosphere. Other unresolved scales are parameterized by adding an iterated Laplacian to the prognostic equations, i. e.,

$$\frac{\partial \psi}{\partial t} = -\tau(-\nabla_{\theta}^2)^{\beta} \psi.$$

Currently, $\beta = 3$, and $\tau = 1.08 \times 10^4 \text{s}^{-1}$. Vertical diffusion of mass and momentum is based on the method used by Hsu and Arakawa (1990).

in an identical fashion. This does not guarantee the absence of negative mixing ratios, and if such regions occur, they are filled in by borrowing ozone pseudo-density from surrounding points. Photochemistry is crudely parameterized as a relaxation towards the climatological fields used by Shine (1987); the relaxation time constant is a function of latitude, altitude and date, based on Garcia and Solomon (1985). Other tracers can also be added to the model.

References

- Andrews, D. G., J. R. Holton, and C. B. Leovy, 1987: *Middle Atmosphere Dynamics*. Academic Press, New York, 489pp.
- Arakawa, A., and V. R. Lamb, 1977: Computational Design of the basic dynamical processes of the UCLA general circulation model. *Methods in Computational Physics*, 17, 174-265.
- Arakawa, A., C. R. Mechoso, and C. S. Konor, 1992: An isentropic vertical coordinate model: Design and application to atmospheric frontogenesis studies. "MAP Special Issue on Mesoscale Modeling -- Meso-Alpha Scale, Numerical Techniques and Models"
- Asselin, R., 1972: Frequency filter for time integrations. *Mon. Wea. Rev.*, **100**, 487-490.
- Baldwin, M. P., and T. J. Dunkerton, 1989: The stratospheric major warming of early December 1987. *J. Atmos. Sci.*, 46, 2863-2884.
- Baldwin, M. P., and J. R. Holton, 1988: Climatology of the stratospheric polar vortex and planetary wave breaking. *J. Atmos. Sci.*, 45, 1123-1142.
- Clough, S. A., N. S. Grahame, and A. O'Neill, 1985: Potential vorticity in the stratosphere derived using data from satellites. *Q. J. Roy. Meteor. Soc.*, **111**, 335-358.
- Dickinson, R. E., 1973: Method of parameterization for infrared cooling between altitudes of 30 and 70 kilometers. *J. Geophys. Res.*, 78, 4451-4457.
- Eliassen, E., B. Machenhauer, and E. Rasmussen, 1970: On a numerical method for integration of the hydrodynamical equations with a spectral representation of the horizontal fields. Institute of Theoretical Meteorology, University of Copenhagen, Report No. 2.
- Fairlie, T. D. A., M. Fisher, and A. O'Neill, 1990: The development of narrow baroclinic

- Fisher, M., 1987: 'The Met.O.20 stratosphere-mesosphere model'. Dynamical climatology Technical Note No. 52. Meteorological Office, Bracknell.
- Fisher, M., A. O'Neill, and R. Sutton, 1993: Rapid Descent of Mesospheric Air in the Stratospheric Polar Vortex. *Geophys. Res. Lett.*, *in press*.
- Garcia, R. R., and S. Solomon, 1985: The effect of breaking gravity waves on the dynamics and chemical composition of the mesosphere and lower thermosphere. *J. Geophys. Res.*, 90, 3850-3868.
- Gelman, M. E., A. J. Miller, K. W. Johnson and R. M. Nagatani, 1986: Detection of long term trends in global stratospheric temperature from NMC analyses derived from NOAA satellite data. *Adv. Space Res.*, 6, No. 10, 17-26.
- Hines, K. M., and C. R. Mechoso, 1991: Frontogenesis processes in the middle and upper troposphere. *Mon. Wea. Rev.*, 119, 1225-1241.
- Holton, J. R., 1976: A semi-spectral numerical model for wave-mean flow interactions in the stratosphere: applications to sudden stratospheric warmings. *J. Atmos. Sci.*, 33, 1066-1069.
- Hoskins, B. J., M. E. McIntyre, and A. W. Robertson, 1985: On the use and significance of isentropic potential vorticity maps. *Quart. J. R. Meteor. Soc.*, 111, 877-946.
- Hsu, Y.-J. G., and A. Arakawa, 1990: Numerical modeling of the atmosphere with an isentropic vertical coordinate. *Mon. Wea. Rev.*, 118, 1933-1959.
- Klenk, K. F., P. K. Bhartia, E. Hilsenrath and A. J. Fleig, 1983: Standard ozone profiles from balloon and satellite datasets. *J. Appl. Meteor.*, 22, 2102-2122.
- Leovy, C. B., C.-R. Sun, M. H. Hitchman, E. E. Remsberg, J. M. Russell III, L. L. Gordley, J. C. Gille, and L. V. Lyjak, 1985: Transport of ozone in the middle stratosphere: Evidence for planetary wave breaking. *J. Atmos. Sci.*, 42, 230-244.
- Manney, G. L., J. D. Farrara, and C. R. Mechoso, 1992: Simulations of stratospheric

- Mechoso, C. R., and A. Arakawa, 1986: Sensitivity of stratospheric forecast to tropospheric forecast. *Short and medium-range numerical weather prediction, collection of papers presented at the WMO/IUGG NWP Symposium*, Tokyo, 4-8 August 1986, 387-395.
- Mechoso, C. R., K. Yamazaki, A. Kitoh, and A. Arakawa, 1985: Numerical forecasts of stratospheric warming events during the winter of 1979. *Mon. Wea. Rev.*, **113**, 1015-1029.
- Newman, P. A., L. R. Lait, M. R. Schoeberl, R. M. Nagatani, and A. J. Krueger, Meteorological Atlas of the Northern Hemisphere Lower Stratosphere for January and February 1989 During the Airborne Arctic Stratospheric Expedition, NASA Tech. Memo. 4145, 185 pp, 1989.
- O'Neill, A., and V. D. Pope, 1988: Simulations of linear and nonlinear disturbances in the stratosphere. *Quart. J. Roy. Meteor. Soc.*, **114**, 1063-1110.
- Orszag, S. A., 1970: Transform method for the calculation of vector-coupled sums: Application to the spectral form of the vorticity equation. *J. Atmos. Sci.*, **27**, 890-895.
- Shine, K. P., 1987: The middle atmosphere in the absence of dynamic heat fluxes. *Quart. J. Roy. Meteor. Soc.*, **113**, 603-633.
- Strobel, D. F., 1978: Parametrization of the atmospheric heating rate from 15 to 120 km due to O₂ and O₃ absorption of solar radiation. *J. Geophys. Res.*, **83**, 9569-9580.
- Suarez, M. J., A. Arakawa, and D. A. Randall, 1983: The parameterization of the planetary boundary layer in the UCLA general circulation model: Formulation and results. *Mon. Wea. Rev.*, **111**, 2224-2243.

Table 1. Summary of forecasts and simulations used for inter-mode] comparisons.

model	start date	boundary data	initial data	length
SMM	15 Feb	NMC	NMC	10 days
ECM	15 Feb	NMC	NMC	10 days
SMM	17 Feb	NMC	NMC	24 days
ECM	17 Feb	NMC	NMC	24 days
ECM	17 Feb	NMC	LIMS	24 days
SMM	15 Feb	FGGE	FGGE+NMC	10 days
SMM	15 Feb	GCM	FGGE+NMC	10 days
GCM	15 Feb	---	FGGE+NMC	10 days
SMM	17 Feb	FGGE	FGGE+NMC	10 days
SMM	17 Feb	GCM	FGGE+NMC	10 days
GCM	17 Feb	---	FGGE+NMC	10 days

Table 2. Entropy Coordinate Model (ECM) simulations used to test various features of the model. With transport on, ozone (O_3) is transported by the model and is interactive with the radiation code. Under radiation, full means the detailed radiation sh=cheme (Shine 1987) is used, Nc means a simple Newtonian cooling is used. "cl O_3 " refers to a climatological zonal mean distribution of O_3 as described in text.

start date	transport (on or off)	radiation (full or Nc)	truncation	levels boundary	lower data	initial
15 Feb	on	full	T30	15	400 K	NMC+cl O_3
	off	full	T30	15	400 K	NMC+cl O_3
	off	full	T30	15	400 K	LIMS+cl O_3
	off	full	T30	15	420 K	LJMS+cl O_3
17 Feb	on	full	T30	15	400 K	NMC+cl O_3
	off	full	T30	15	400 K	NMC+cl O_3
	off	full	T30	20	400 K	NMC+cl O_3
	on	full	T30	15	400 K	LIMS+cl O_3
	off	full	T30	15	400 K	LIMS+cl O_3
	off	full	T30	15	420 K	LIMS+cl O_3
	on	full	T30	15	400" K	LIMS+LIMS O_3
	off	Nc	T30	15	400 K	LIMS
	off	Nc	T60	30	400 K	LIMS

Figure and Table Captions

Figure 1. Geopotential heights (grey scale, km) and temperatures (contours, K) from LIMS data at 10 mb, every two days from 17 Feb 1979 through 11 Mar 1979. Projection is polar stereographic, with outer edge at 20°N latitude. 30° and 60° latitude circles are shown as dashed lines.

Figure 2, Longitude/height plot at 60°N latitude of LIMS temperatures (K) for 25 Feb 1979.

Figure 3. Rossby-Ertel potential vorticity (Q) calculated from LIMS data on the 850 K isentropic surface (a) 21 Feb 1979, (b) 25 Feb 1979, (c) 27 Feb 1979, (d) 1 Mar 1979, (e) 3 Mar 1979, and (f) 11 Mar 1979. Units of Q are $10^{-4} \text{ K}^2 \text{ m}^{-1} \text{ kg}^{-1} \text{ s}^{-1}$.

Figure 4. Geopotential heights (grey scale) and temperatures (contours) at 10 mb for SMM (a and b) and ECM (c and d) simulations started from 17 February using NMC data for initialization, on 21 and 25 February. Units and layout are as in Fig. 1.

Figure 5. Longitude/height plots of temperature at 60°N for SMM (a) and ECM (b) simulations started from 17 February using NMC data for initialization, on 23 February.

Figure 6. Rossby-Ertel potential vorticity (Q) on 21, 23 and 25 February from SMM (a, b, and c) and ECM (d, e, and f) from simulations started on 17 February using NMC data for initialization. Units of Q are $10^{-4} \text{ K}^2 \text{ m}^{-1} \text{ kg}^{-1} \text{ s}^{-1}$.

Figure 7. Geopotential heights (grey scale) and temperatures (contours) at 10 mb for ECM simulation started from 17 February using LIMS data for initialization, on 21 and 25 February. Units and layout are as in Fig. 1.

Figure 8. Longitude/height plots of temperature at 60°N for ECM simulation started from 17 February using LIMS data for initialization, on 23 February.

Figure 10. Vertical velocities (cm s^{-1}) from simulations started on 17 February, for SMM and ECM initialized with NMC data, and ECM initialized with LJMS data. (a) through (c) show longitude/height cross-sections at 60°N ; (d) through (f) show horizontal cross-sections at 12.2 mb (level marked on vertical sections).

Figure 11. (a) through (d) Geopotential heights (grey scale) and temperatures (contours) at 10 mb for SMM (a and b) and ECM (c and d) simulations started from 17 February using NMC data for initialization, on 5 and 11 March. Units and layout are as in Fig. 1. (e) through (h) Rossby-Ertel potential vorticity (Q) on 21, 23 and 25 February from SMM (e and f) and ECM (g and h) from simulations started on 17 February using NMC data for initialization. Units of Q are $10^{-4} \text{ K}^2 \text{ m}^{-1} \text{ kg}^{-1} \text{ s}^{-1}$.

Figure 12. Geopotential heights (grey scale) and temperatures (contours) at 10 mb for mini-ECM runs started from 17 February with a T30 truncation and 15 levels (a and b) and with T60 truncation and 30 levels (c and d), on 21 and 25 February. Units and layout are as in Fig. 1.

Figure 13. Longitude/height plots of temperature at 60°N for T30 (a and b) and T60 (c and d) mini-ECM runs, on 23 and 25 February.

Figure 14. Three-dimensional plots representing the structure of the polar vortex during the warming, from the ECM simulation started from 17 February using NMC data for initialization. The lowest level is 470 K, the highest 1700 K. The outer white sulfate shows values of Q in vorticity units (see text) of 1.65 s^{-1} ; the inner blue surface shows temperatures less than 200 K. The colored plot at the bottom shows Q on the 874 K isentropic surface, in the center of the vertical range shown. 40° , 60° , and 80° latitude circles are shown, and 0° and 90°E longitudes are labeled. Plots are for every two days from 17 February through 5 March.

Figure 15. Longitude/height cross-sections at 60°N of temperatures (grey scale, K) and vertical velocities (contours, cm s^{-1}) from the, ECM simulation started from 7

Figure 16. Horizontal plots at 12.2 mb of temperatures (grey scale, K) and vertical velocities (contours, cm s^{-1}) from the ECM simulation started from 17 February using LIMS data for initialization, every two days for 19 through 27 February.

Figure 17. Schematic of the structure of one polar vortex at the peak of the warming (see text).

Figure 18. Trajectories from the ECM simulation starting 17 February initialized with LIMS data. Five trajectories started at 850 K and 30°N . Symbols are plotted every day; trajectory positions were saved every 4 hours. (a) horizontal positions; the field in the background is Q at 850 K on 21 February. (b) pressure as a function of time. (c) e as a function of time.

Figure 19. Trajectories from the ECM simulation starting 17 February initialized with LIMS data. Five trajectories started at 850 K and 70°N . Symbols are plotted every day; trajectory positions were saved every 4 hours. (a) horizontal positions; the field in the background is Q at 850 K on 23 February. (b) pressure as a function of time. (c) θ as a function of time.

Figure 20. (a) through (d) Ozone mass mixing ratio at 850 K from the ECM simulation starting 17 February initialized with LIMS data. Every 4 days for 17 February through 1 March. (e) through (h) Ozone mass mixing ratio for the same days from LIMS data.

Figure 20. (a) through (d) Ozone mass mixing ratio at 60°N from the ECM simulation starting 17 February initialized with LIMS data. Every 4 days for 17 February through 1 March. (e) through (h) Ozone mass mixing ratio for the same days from LIMS data.

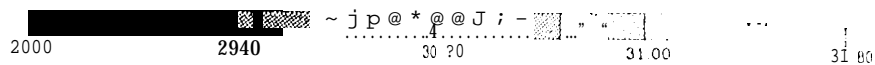
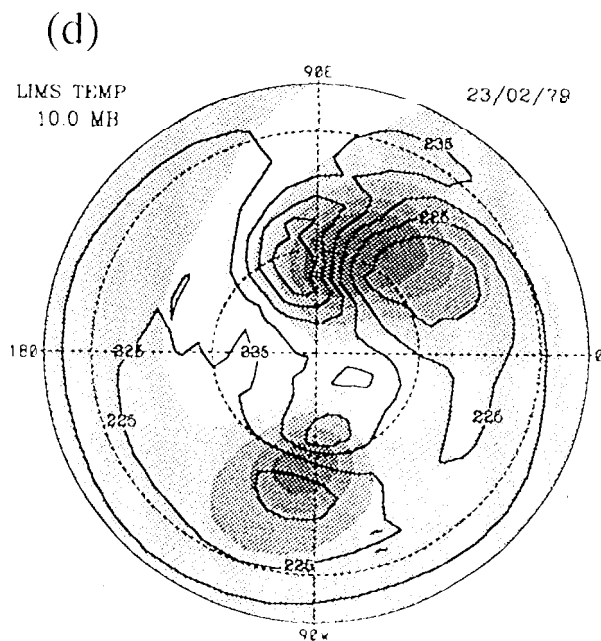
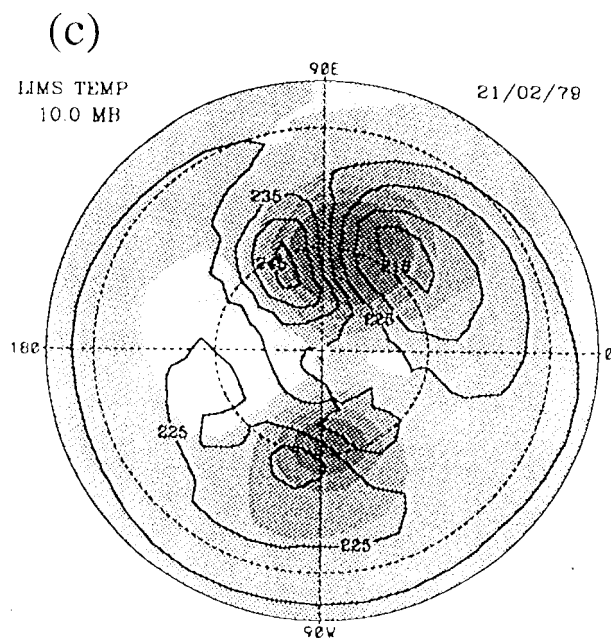
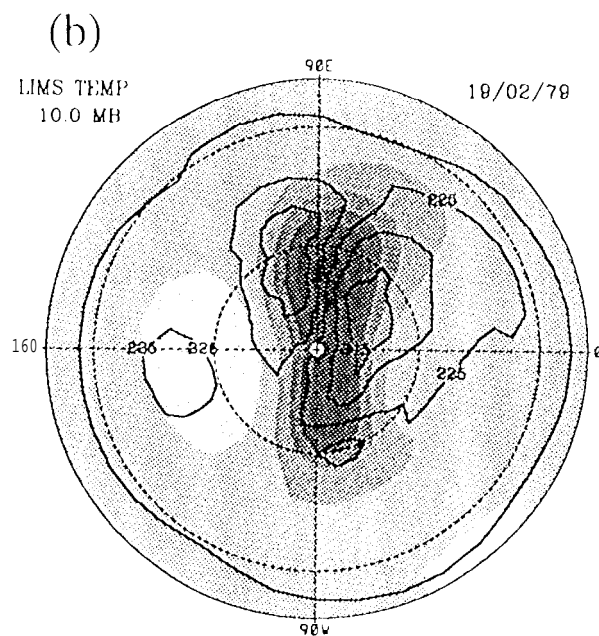
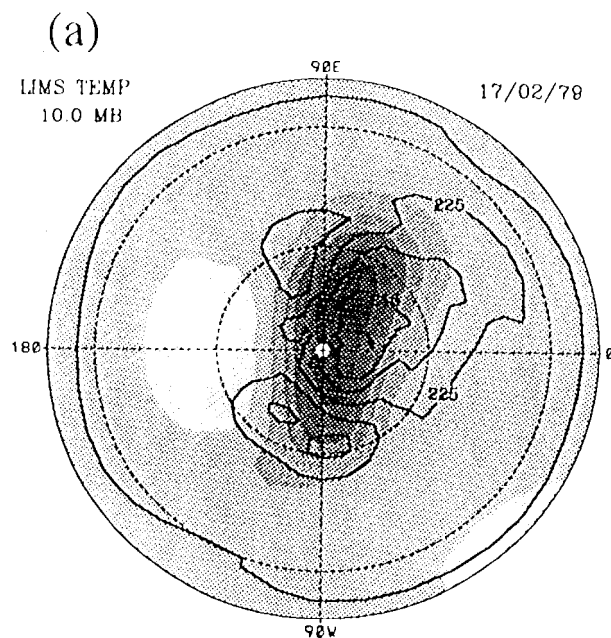
Figure 22. Geopotential heights (km) from the SMM simulation initialized on 15 February using FGGF data for boundary fields and initialization, on 21 and 25 February.

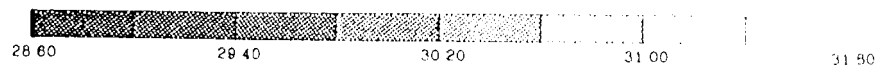
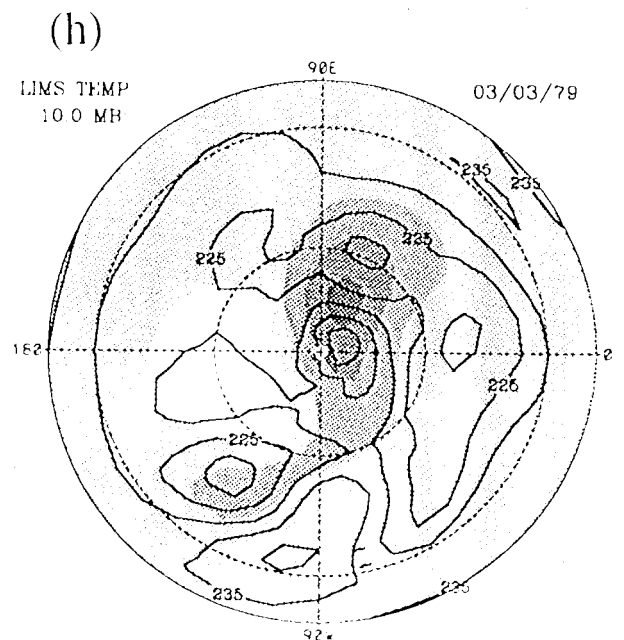
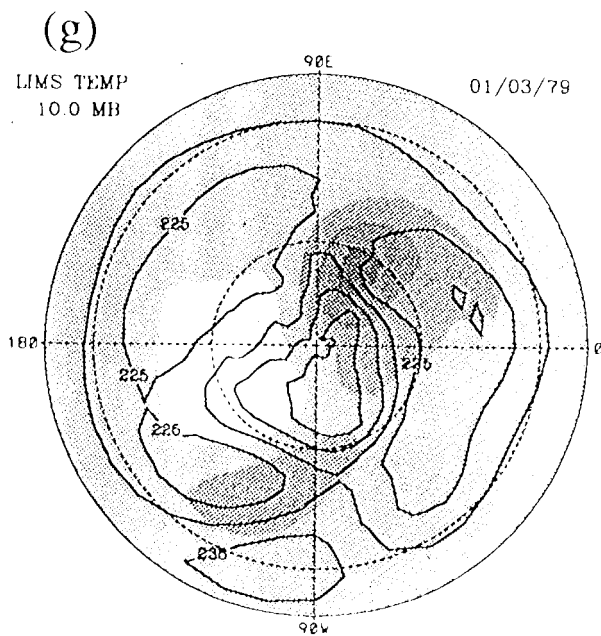
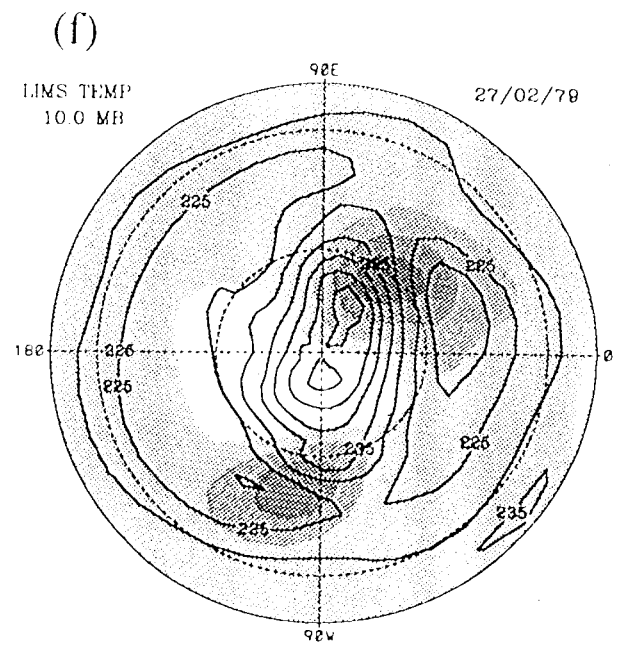
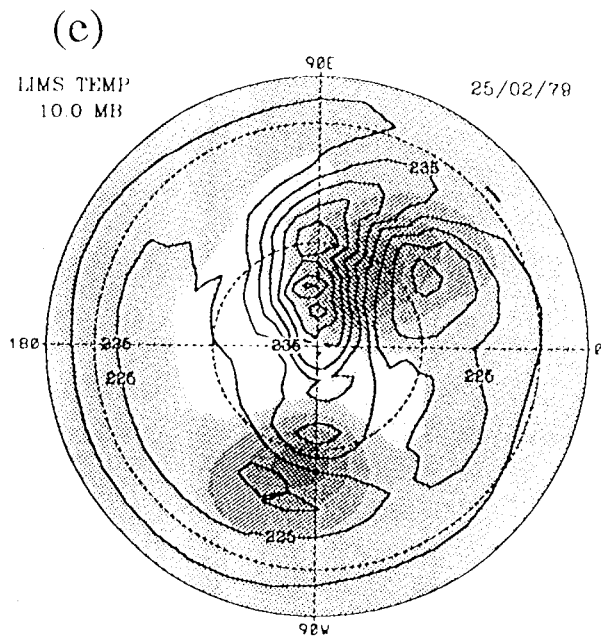
21 and 25 February are shown.

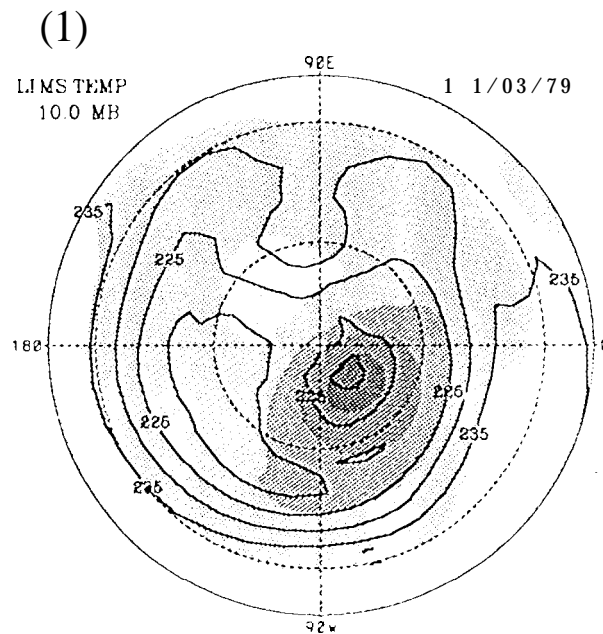
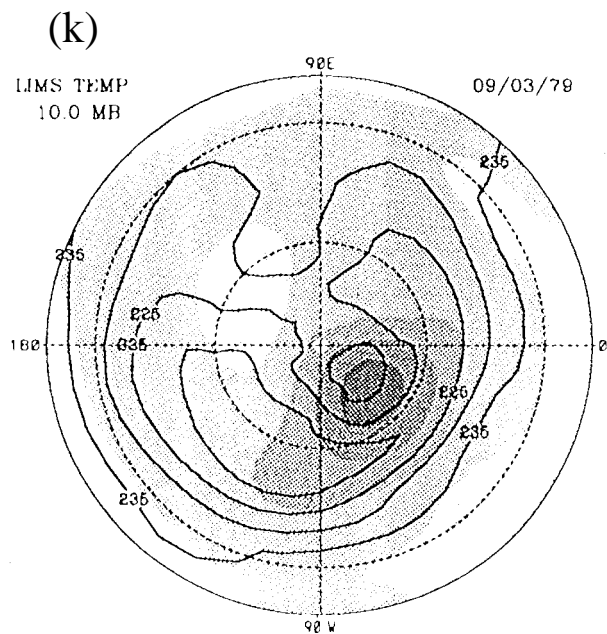
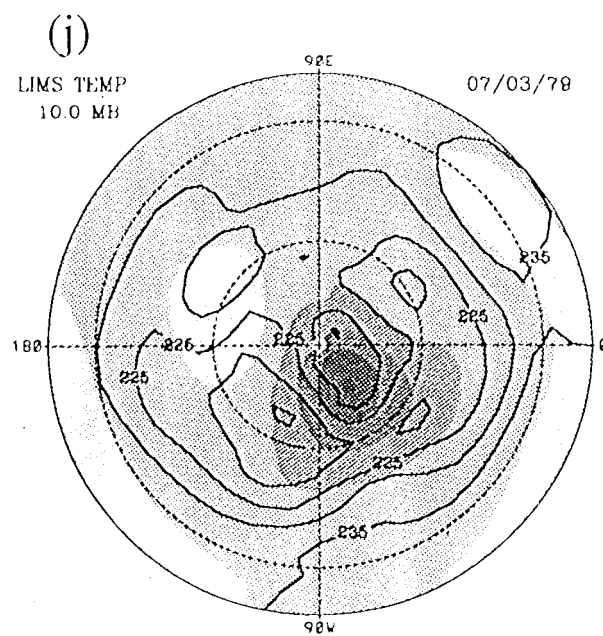
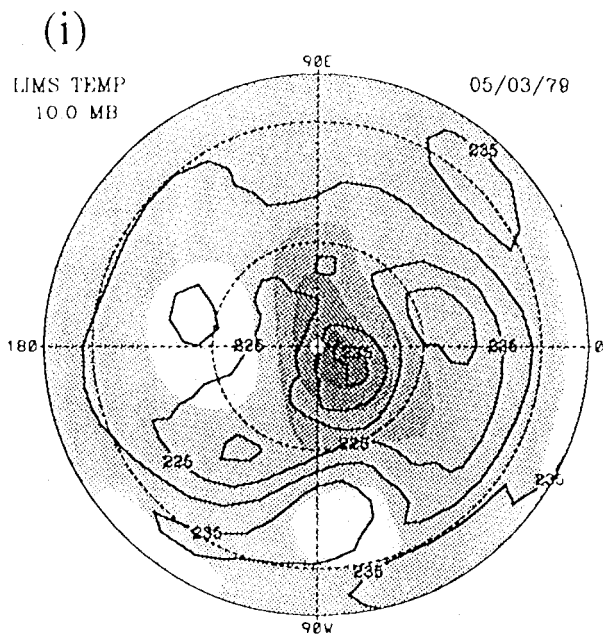
Figure 24. Longitude/height plots of temperature at 60°N on 23 February from (a) the GCM forecast initialized on 17 February, (b) the SMM simulation started on 17 February using 100 mb heights from the GCM forecast for boundary fields, and (c) the SMM simulation started on 17 February using FGGE data for initialization and boundary fields.

Table 1. Summary of forecasts and simulations used for inter-model comparisons.

Table 2. Entropy Coordinate Model (ECM) simulations used to test various features of the model. With transport on, ozone (O_3) is transported by the model and is interactive with the radiation code. Under radiation, full means the detailed radiation scheme (Shine 1987) is used, Nc means a simple Newtonian cooling is used. "cl O_3 " refers to a climatological zonal mean distribution of O_3 as described in text.





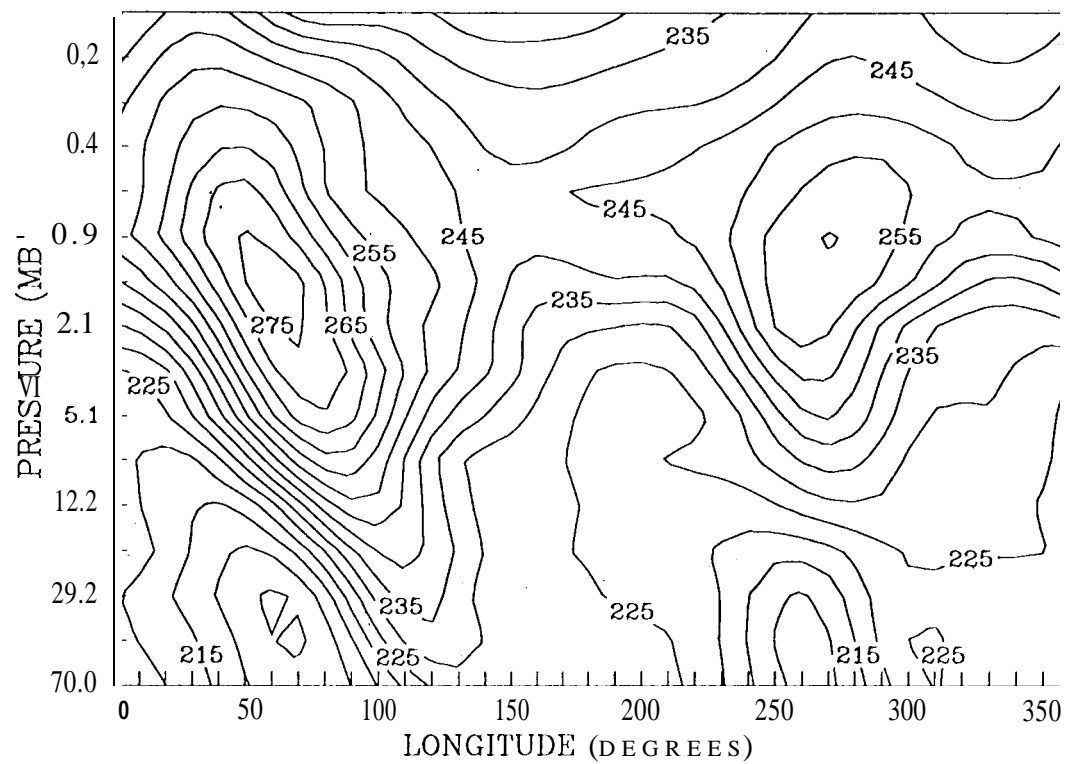


3: 50

17.1

LIMS TEMP

25/02/79



CONTOUR FROM 200 TO 300 BY 5

Fig. 2

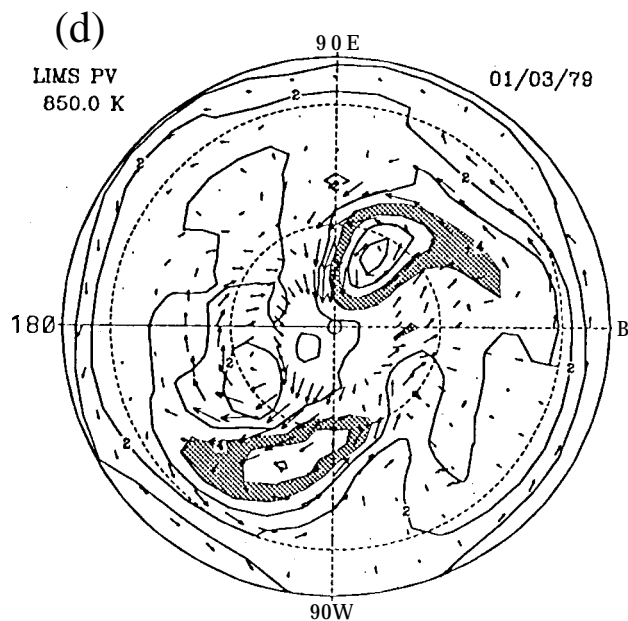
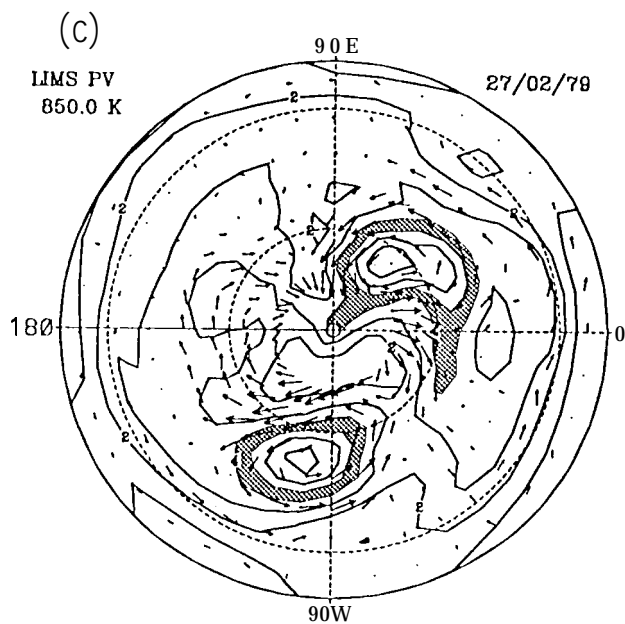
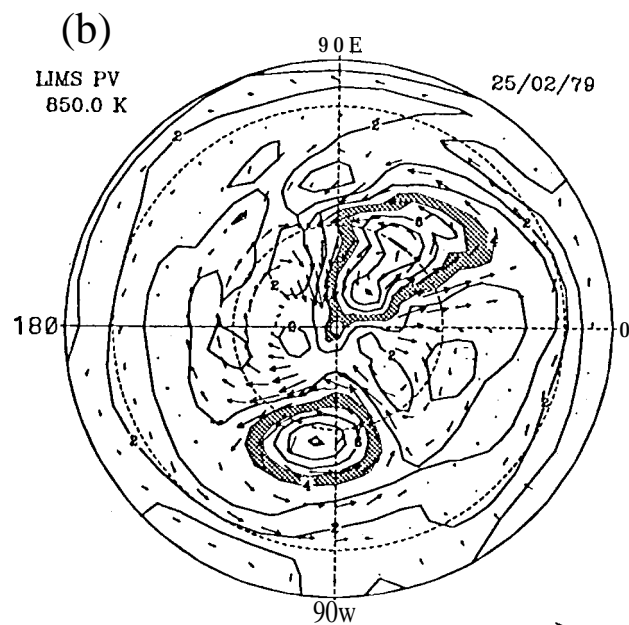
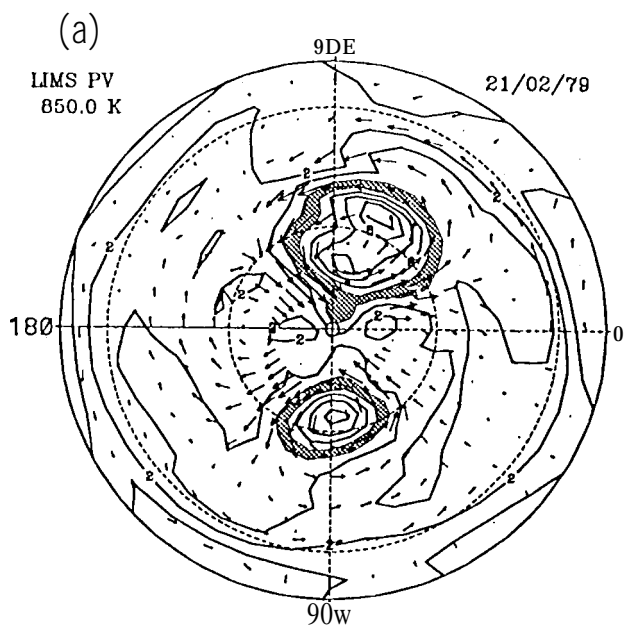


Fig. 3

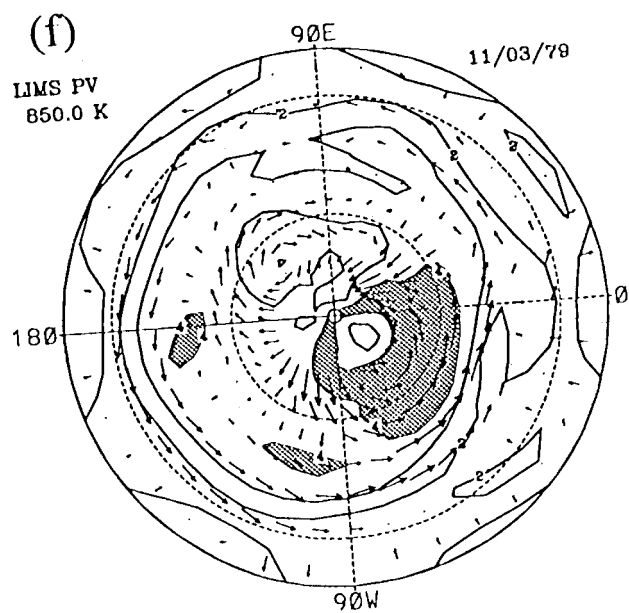
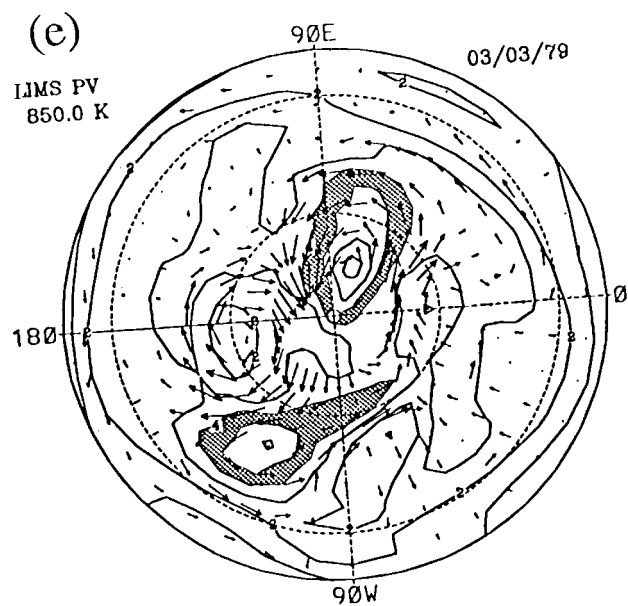
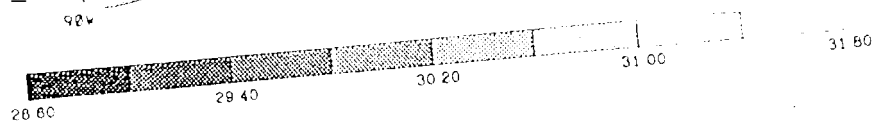
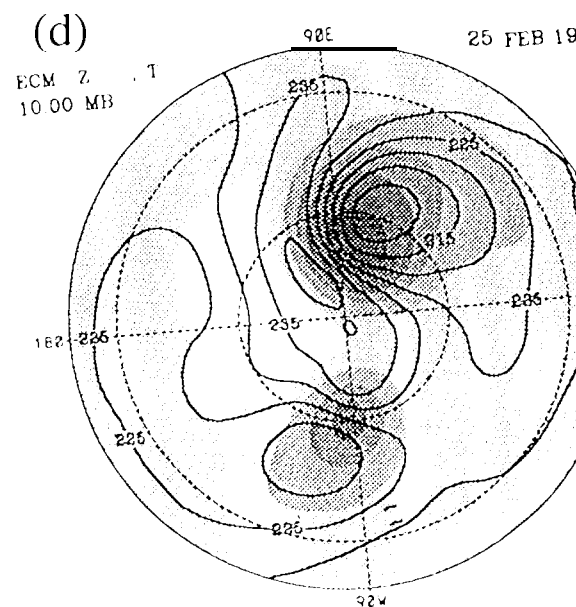
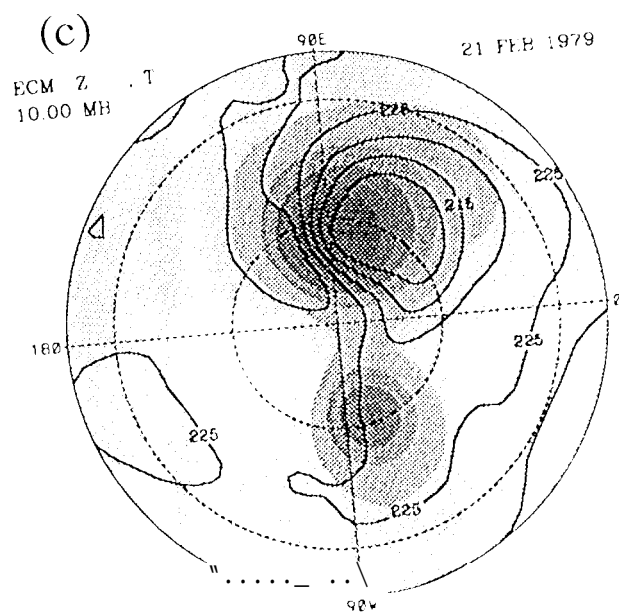
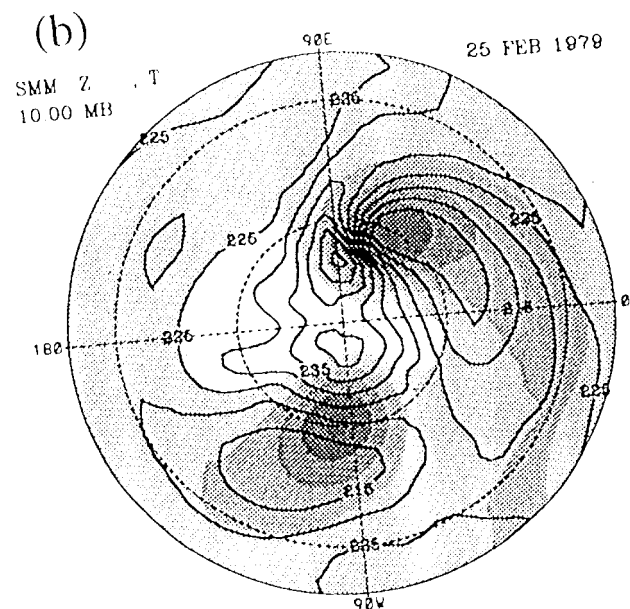
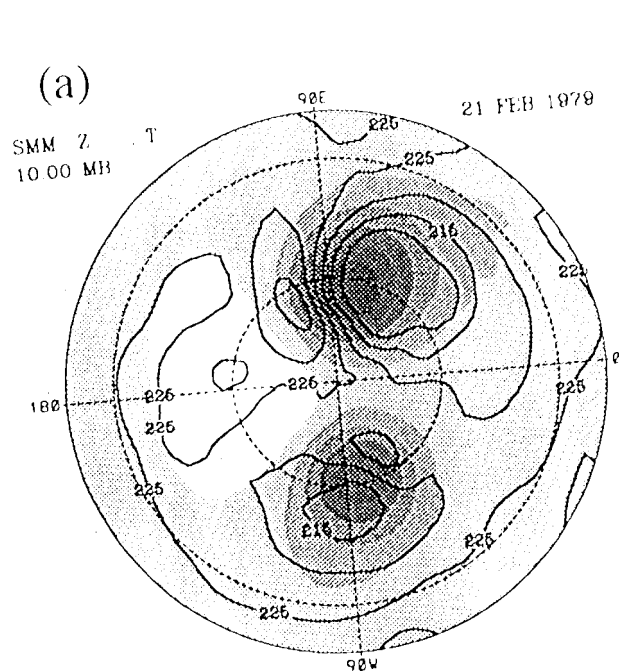


Fig. 3



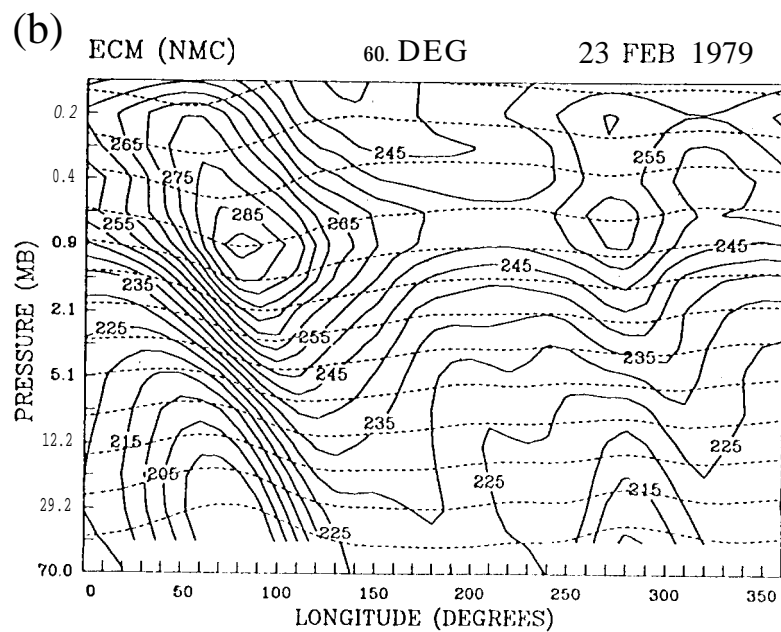
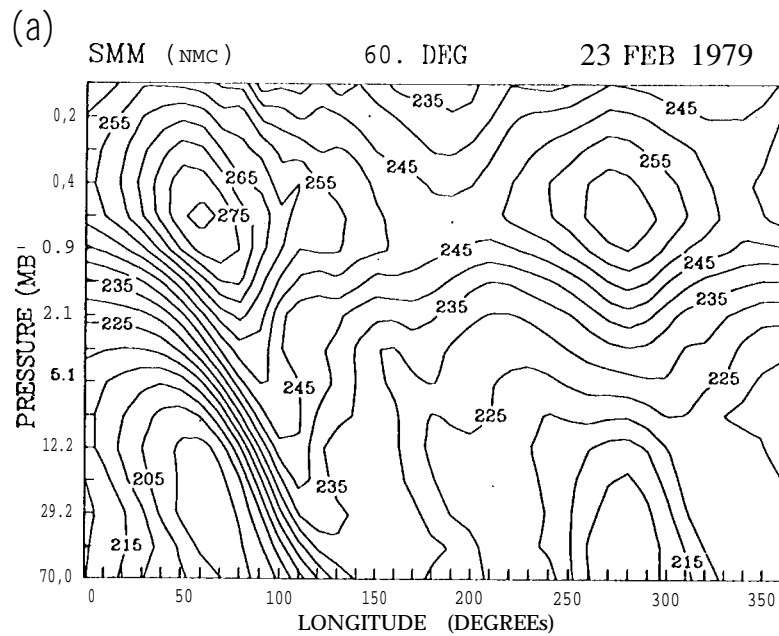
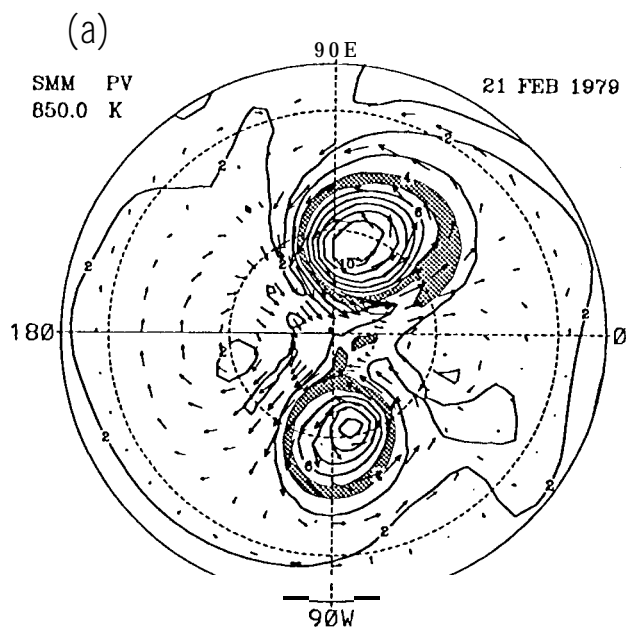
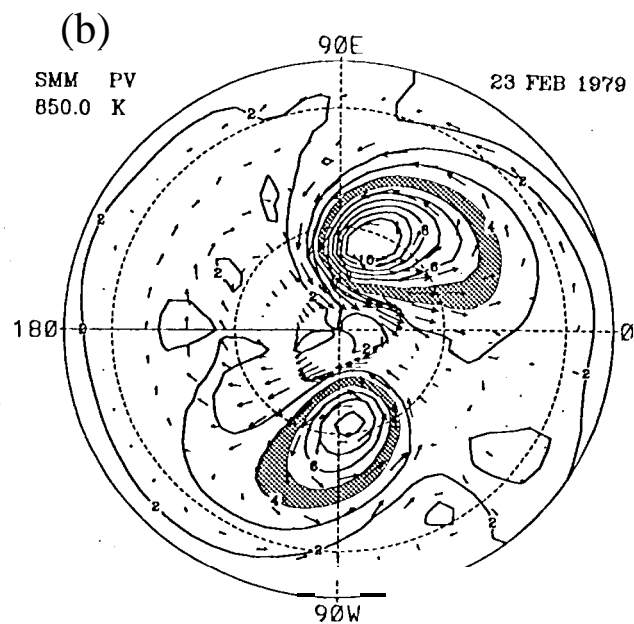


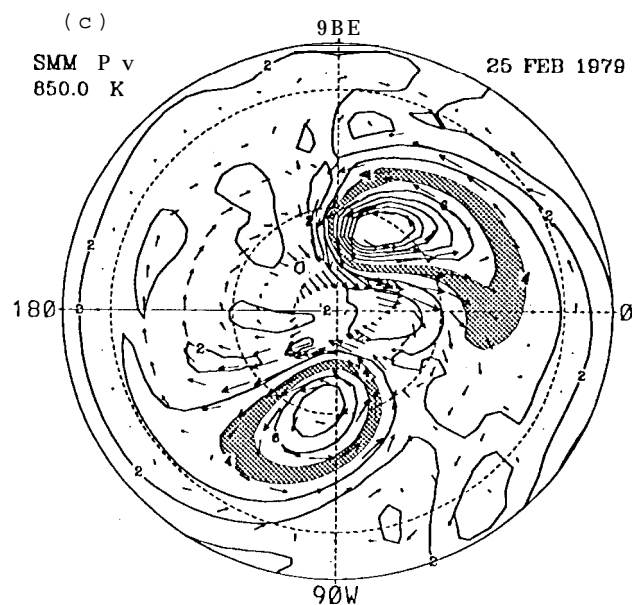
Fig. 5



CONTOUR FROM 1 TO 10 BY 1



CONTOUR FROM 1 TO 10 BY 1



CONTOUR FROM 1 TO 10 BY 1

Fig. 6

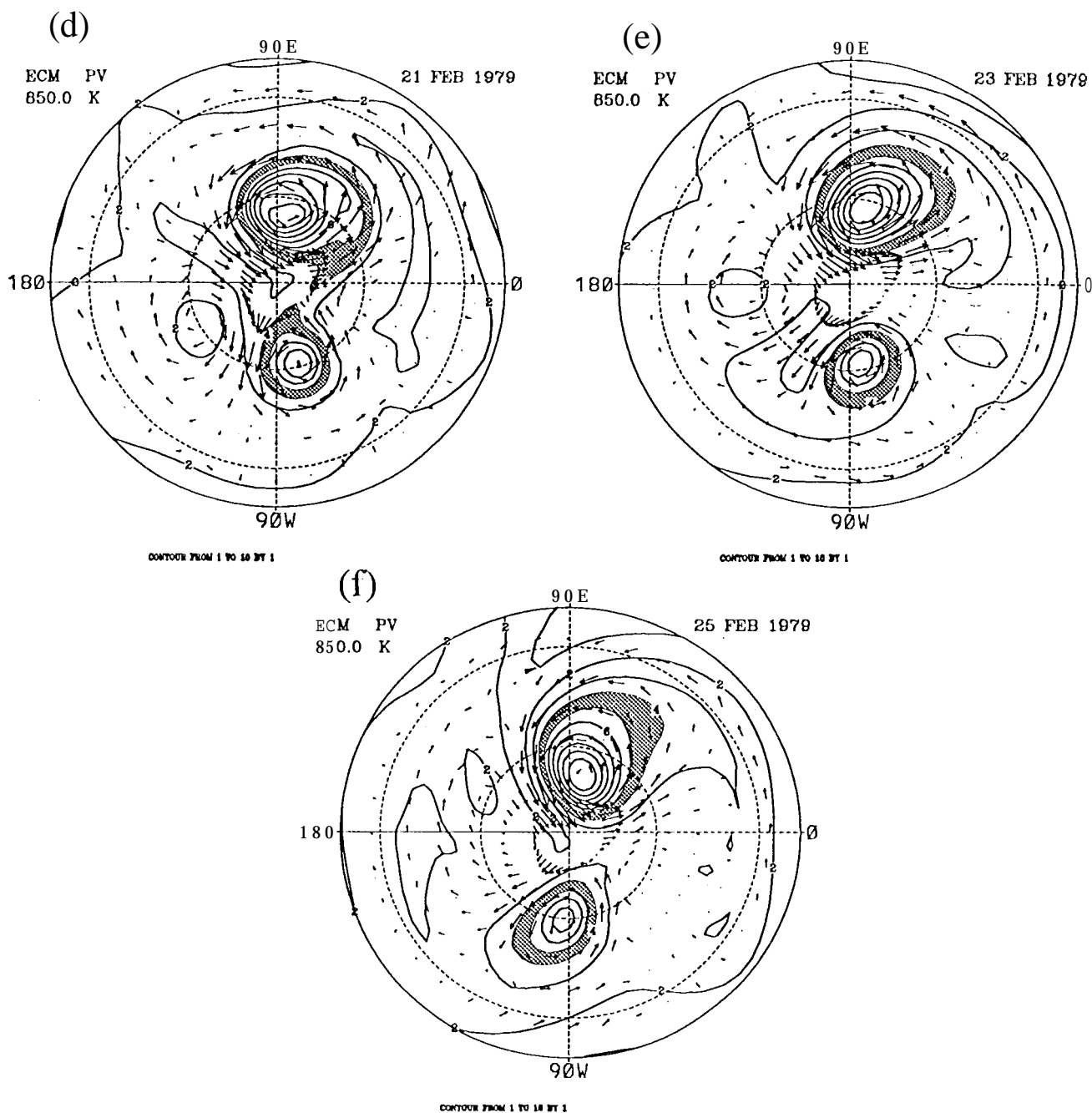


Fig. 6

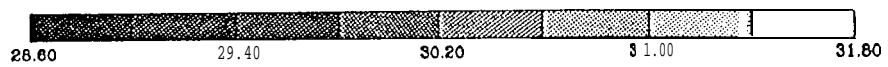
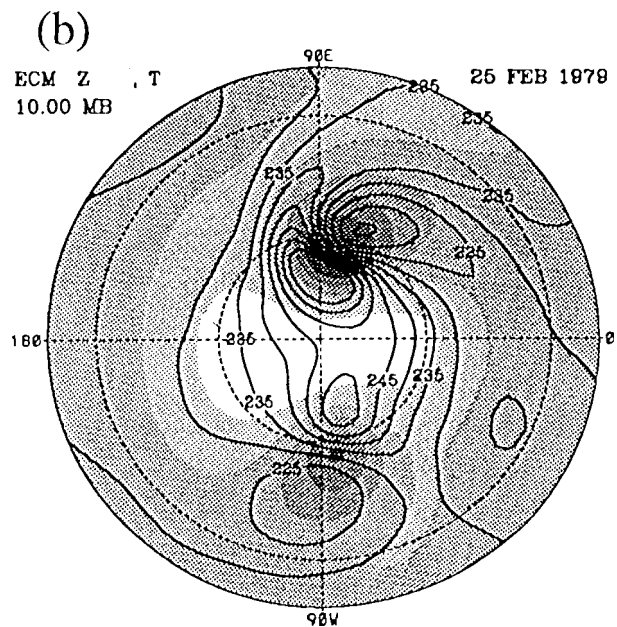
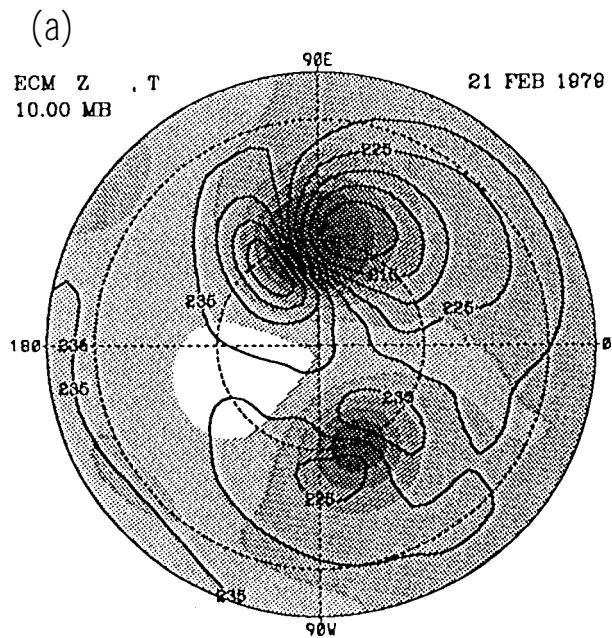


Fig. 7

ECM

60. DEG

23 FEB 1979

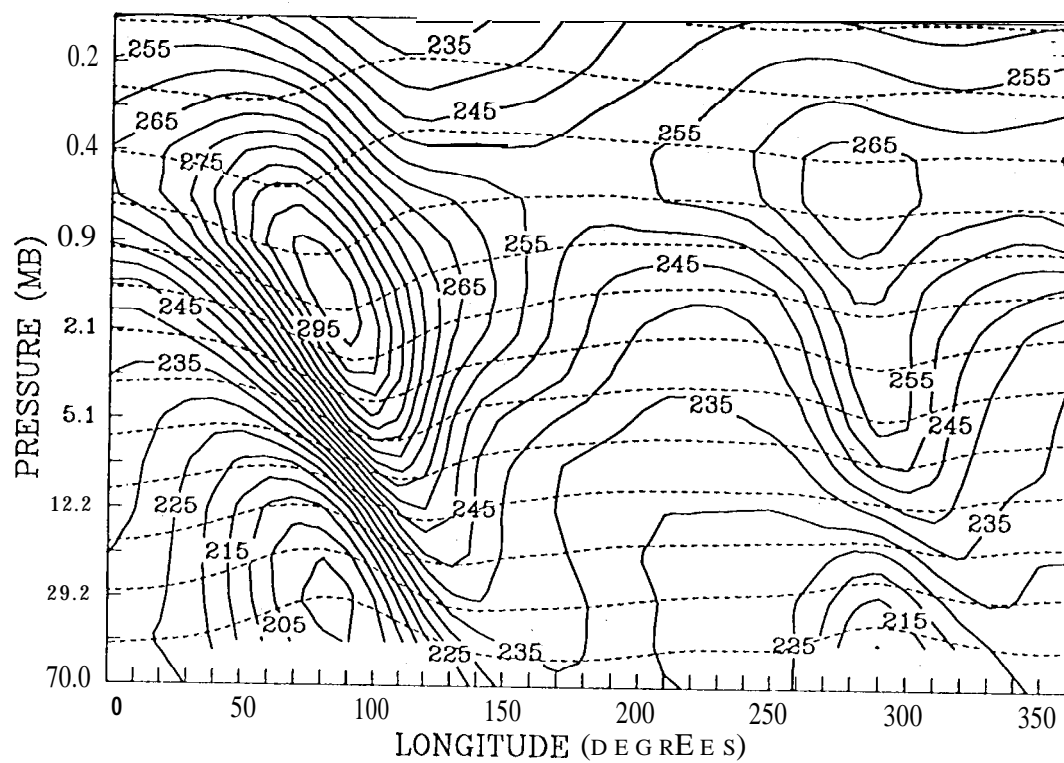


Fig. 8

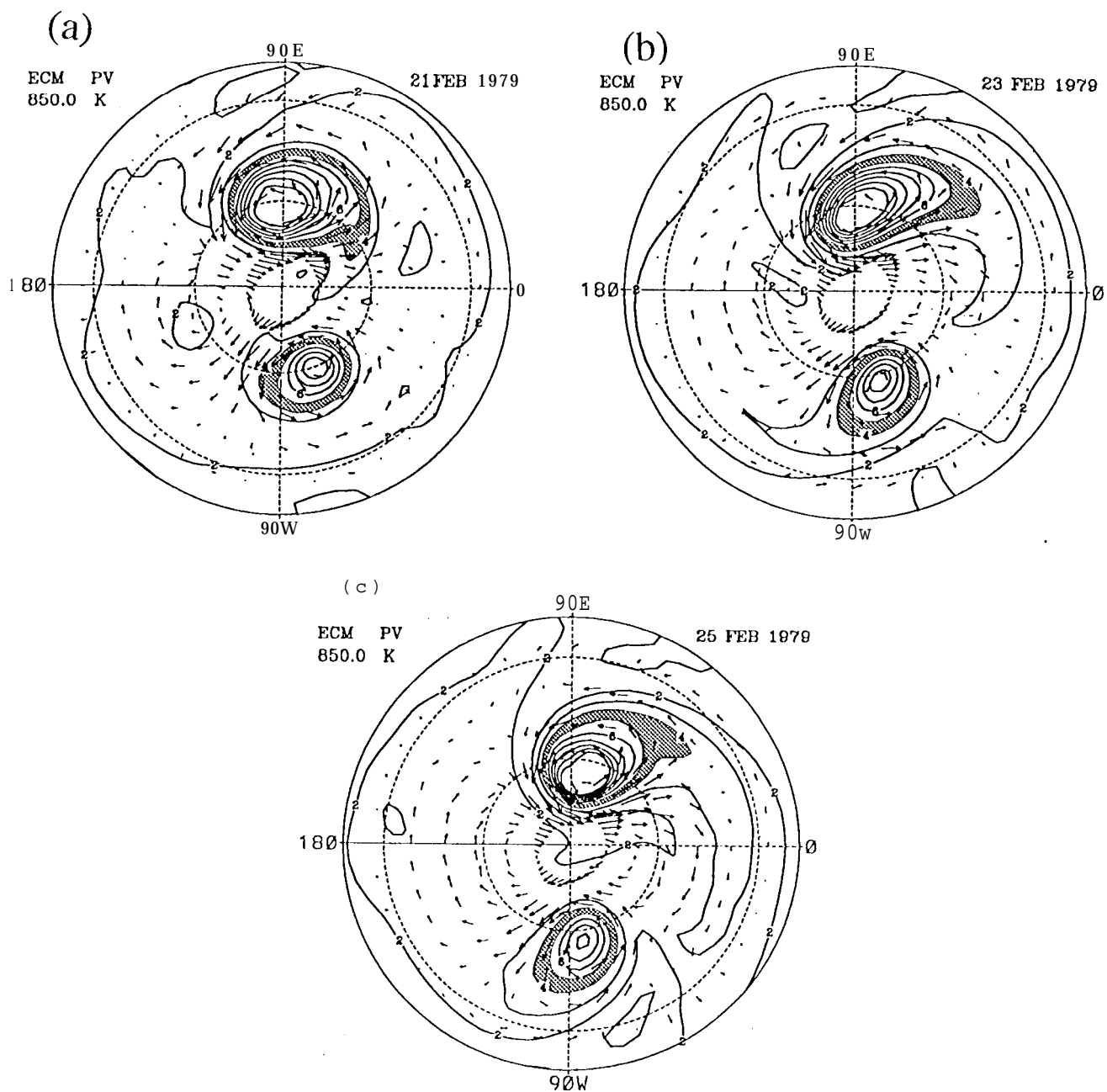


Fig. 9

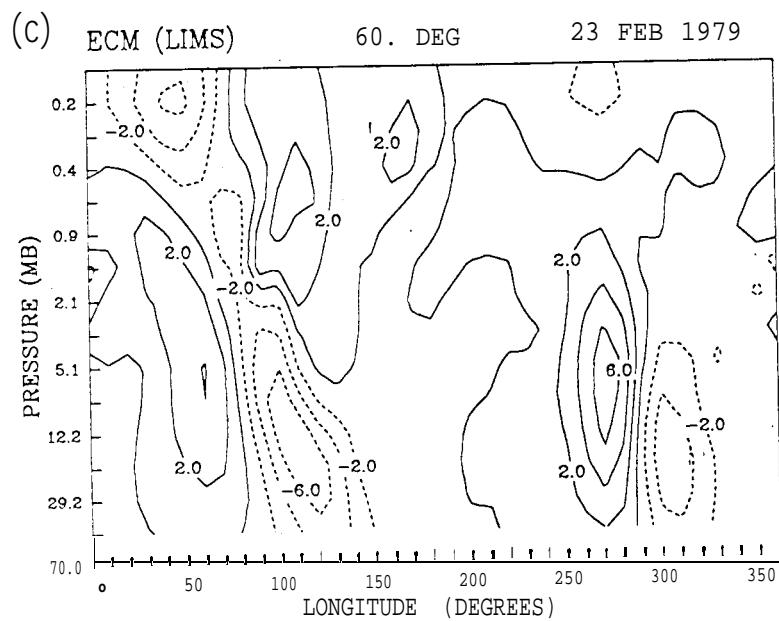
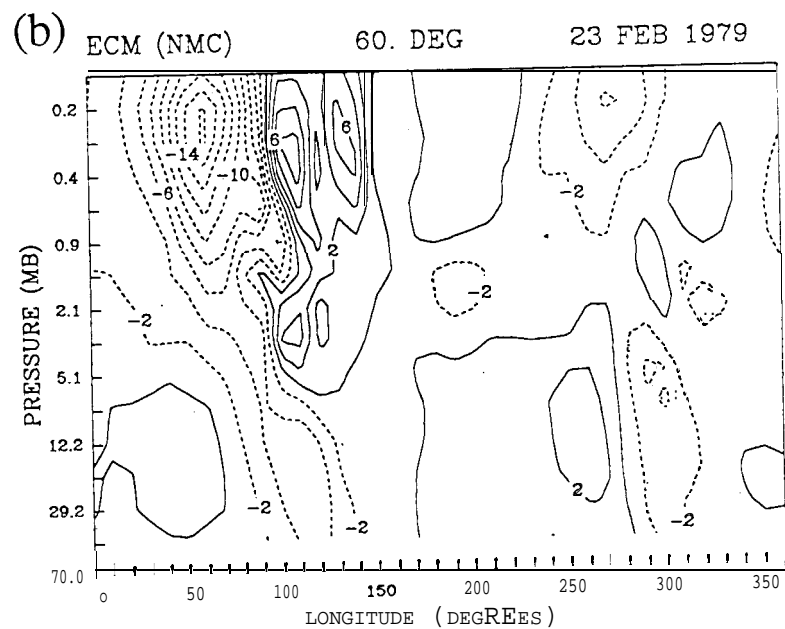
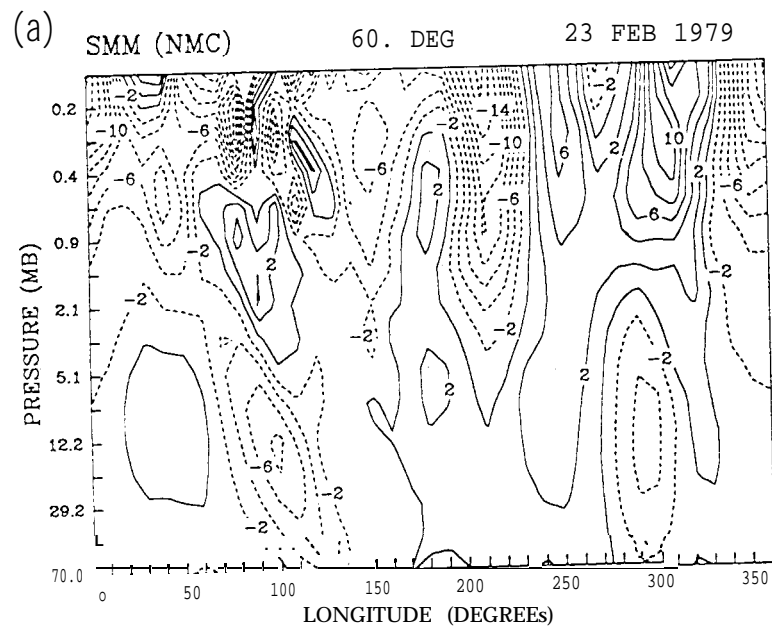


Fig. 10

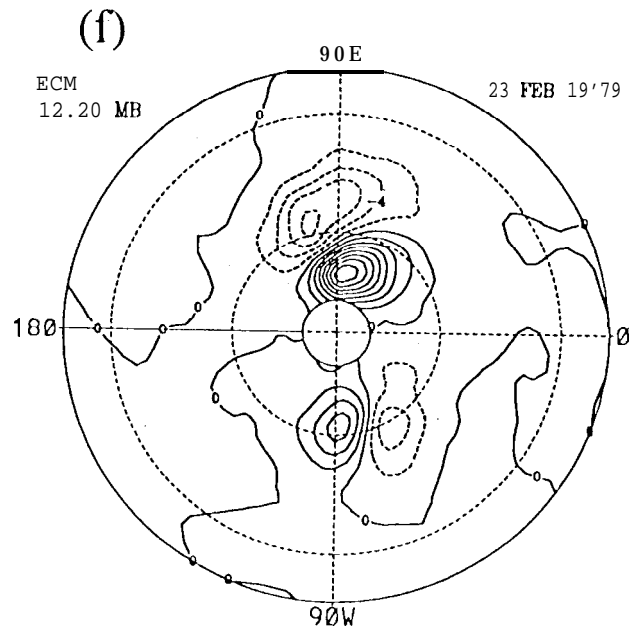
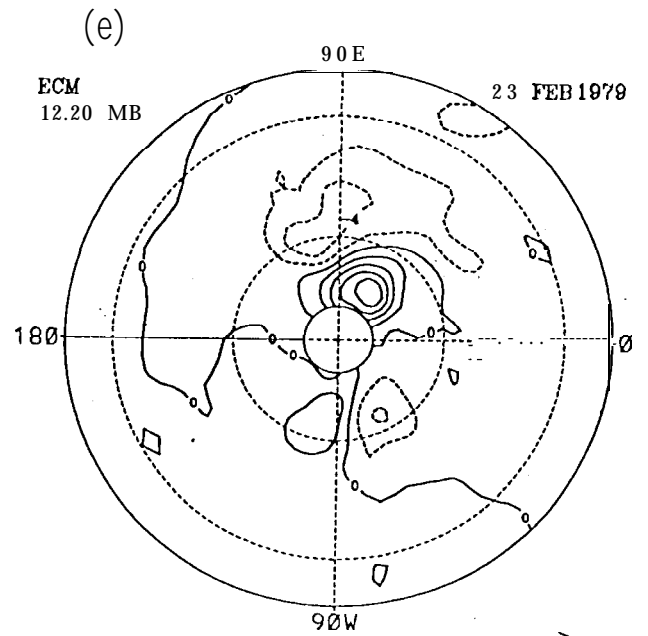
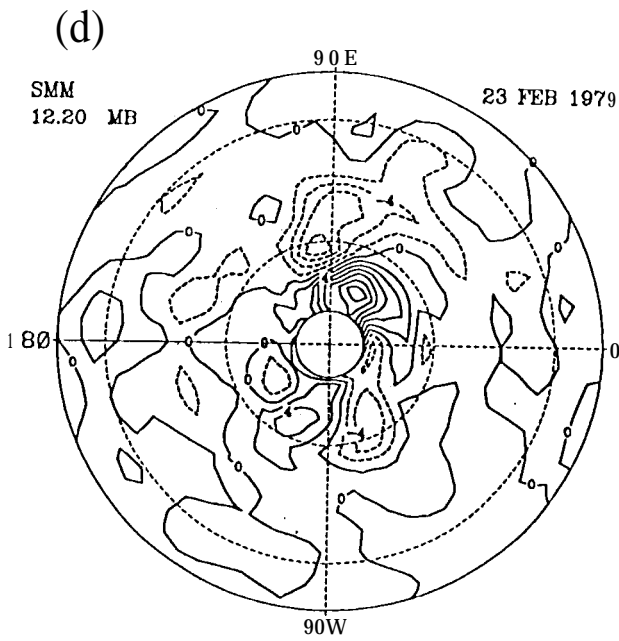
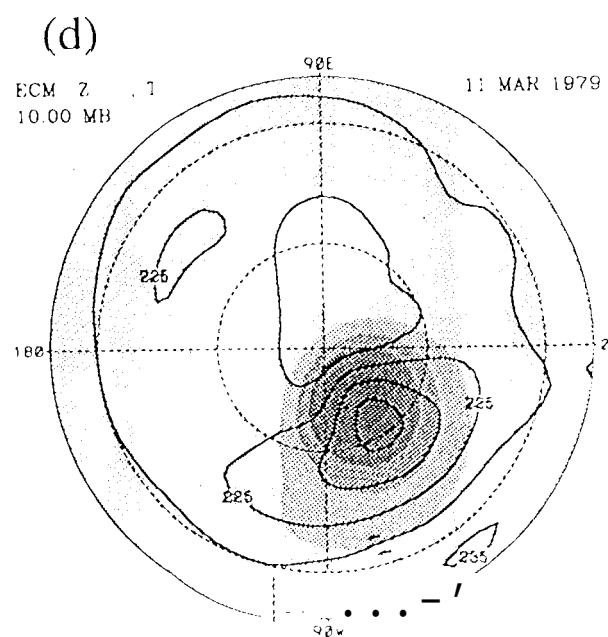
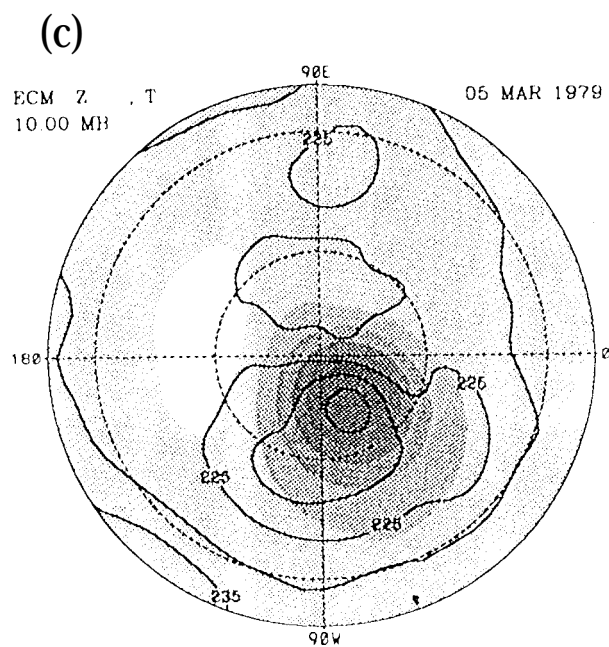
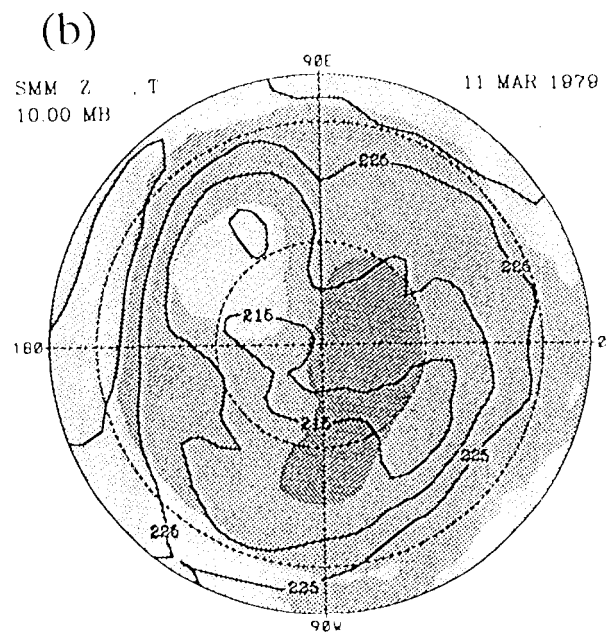
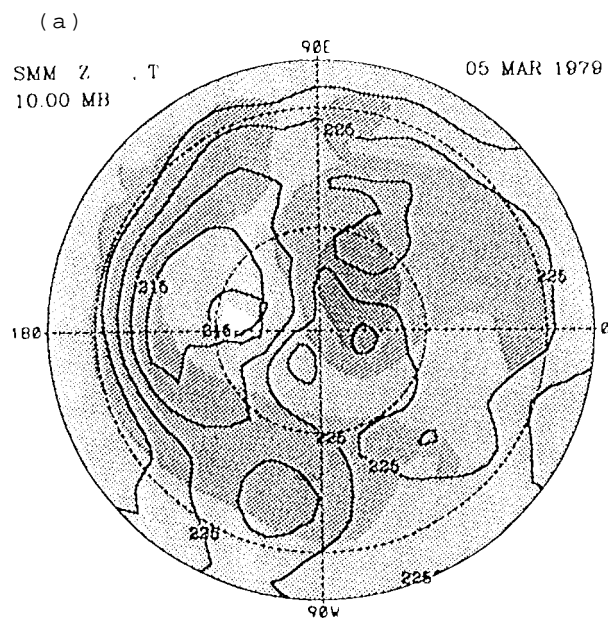


Fig. 10



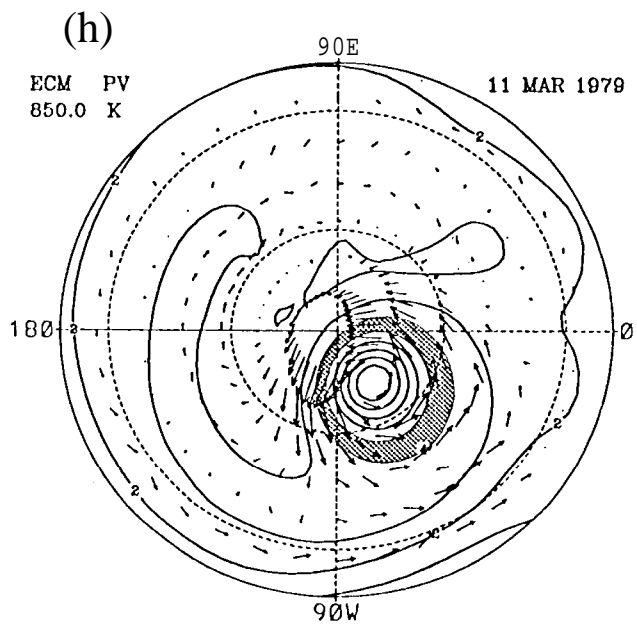
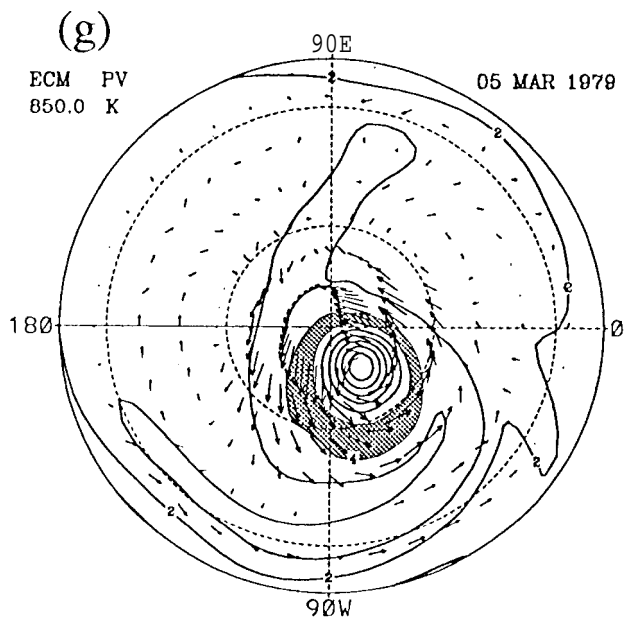
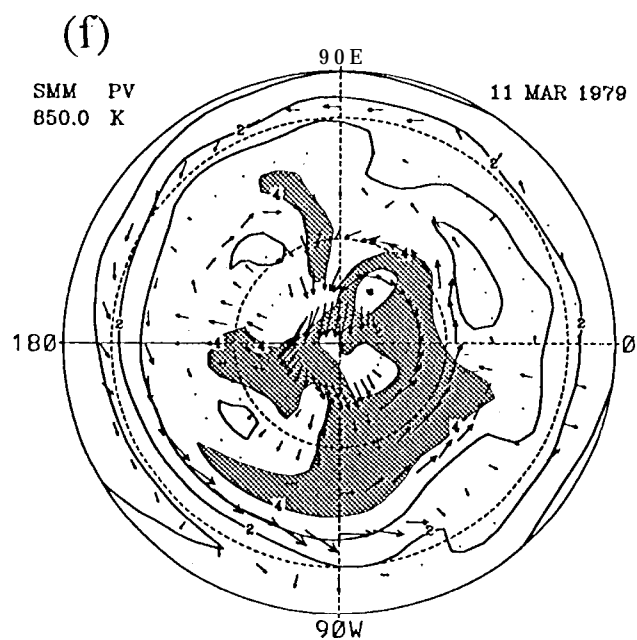
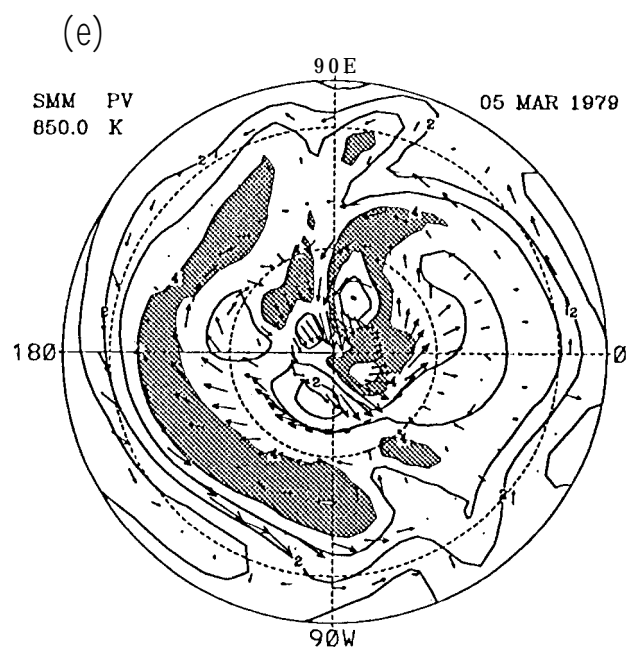
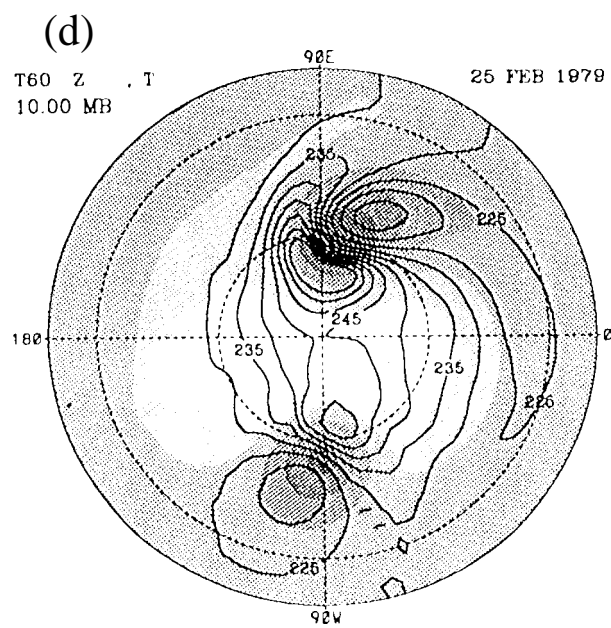
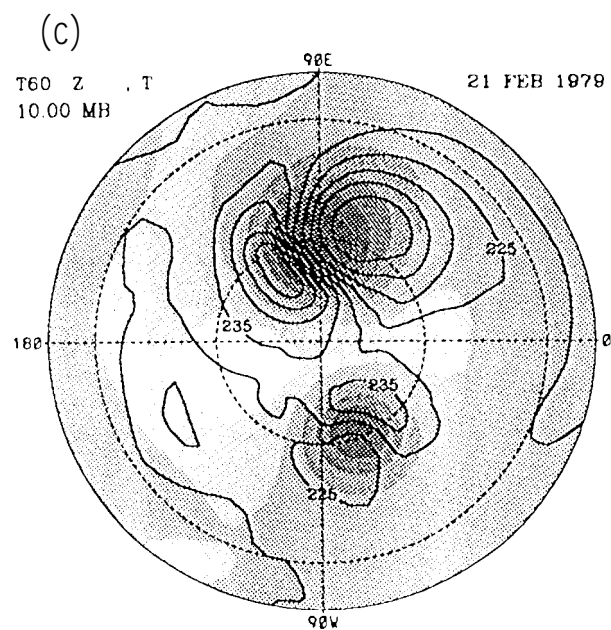
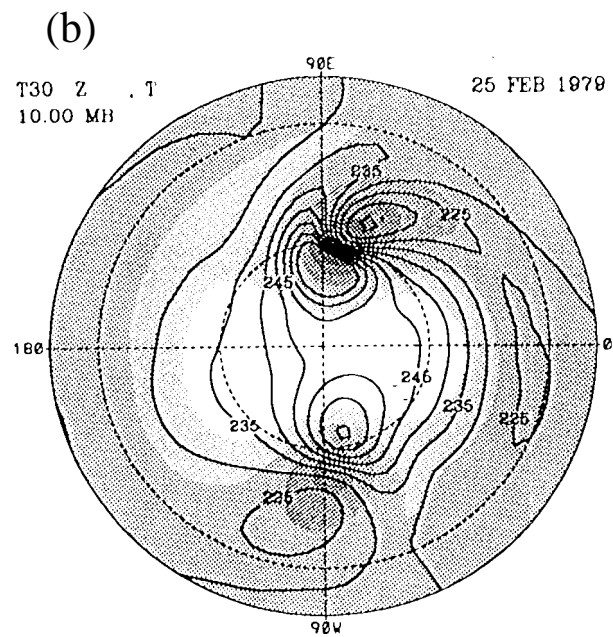
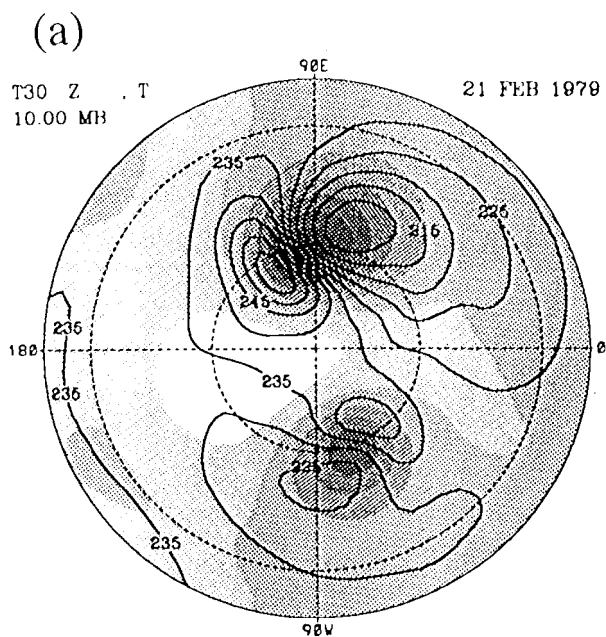


Fig. 11



17-172

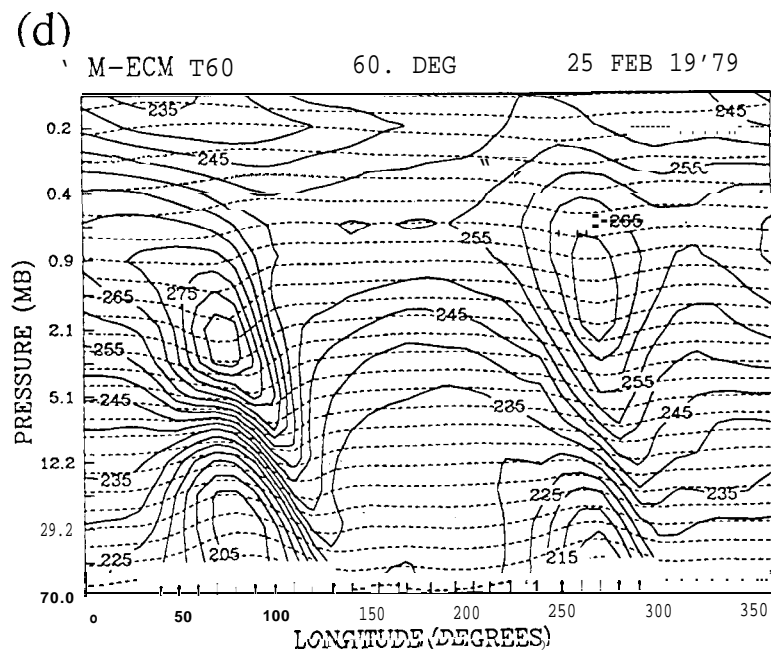
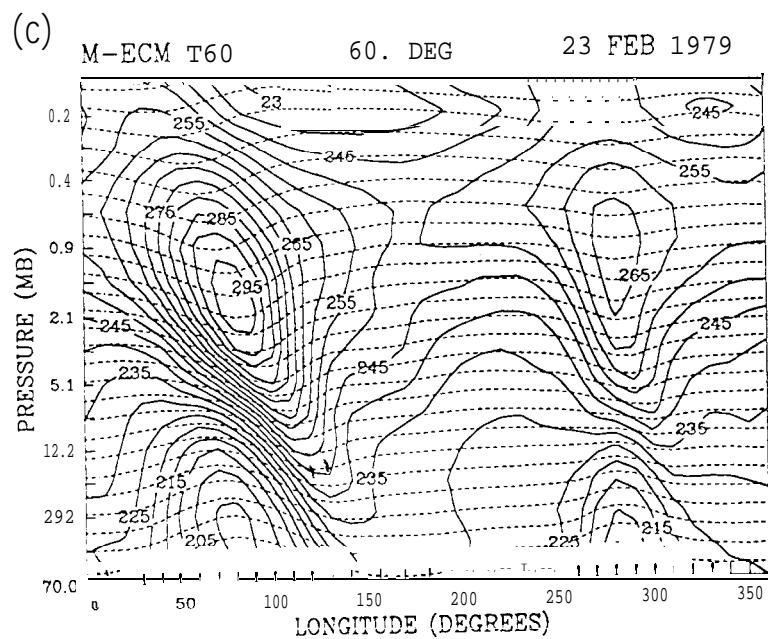
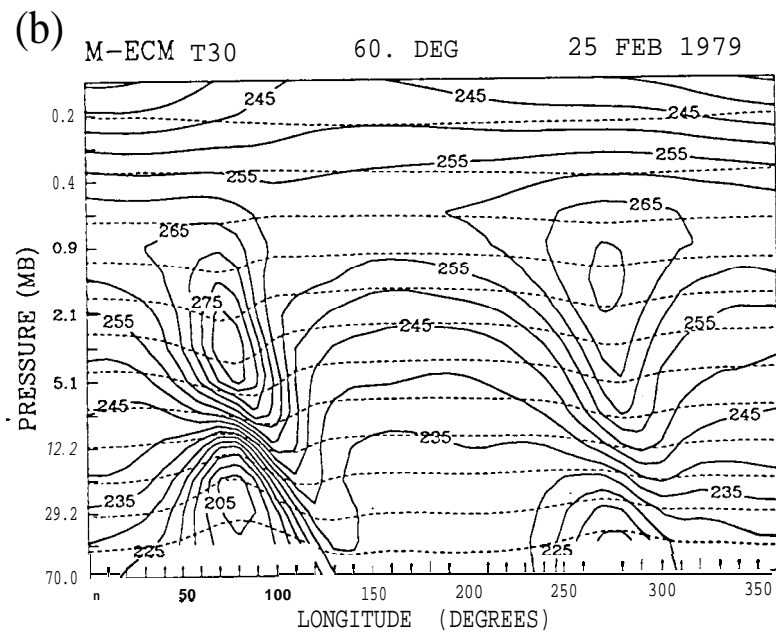
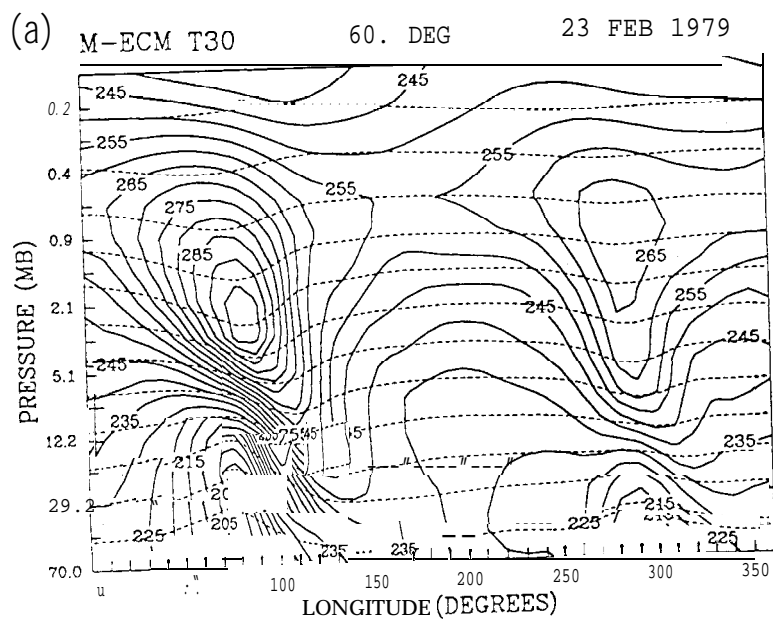
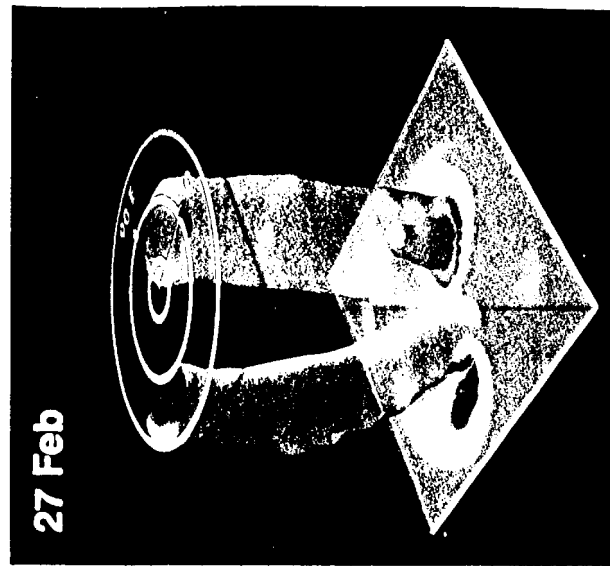
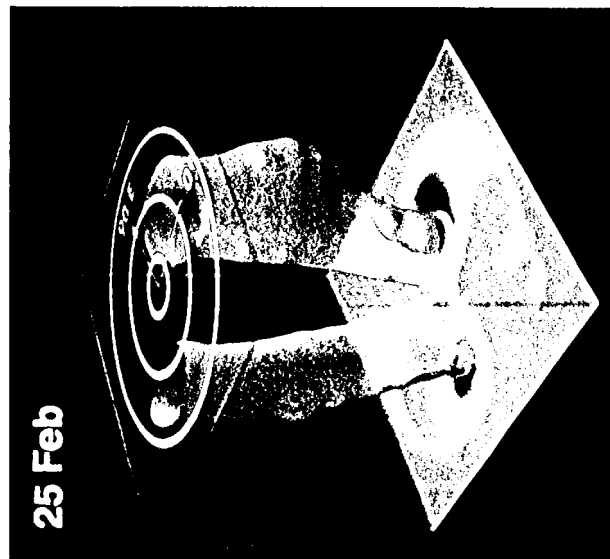
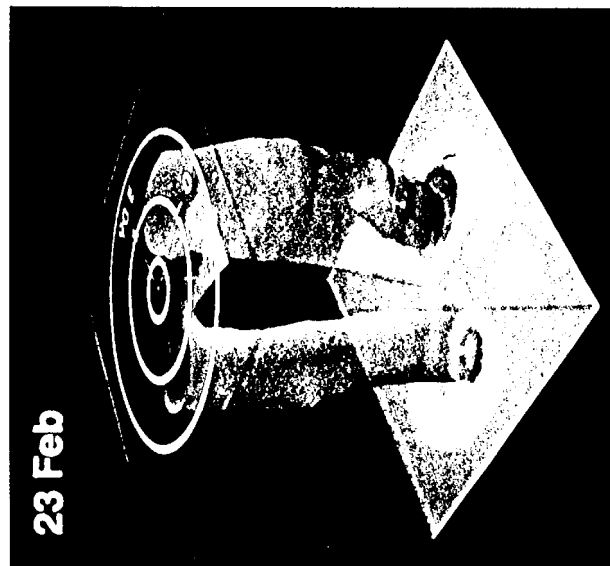
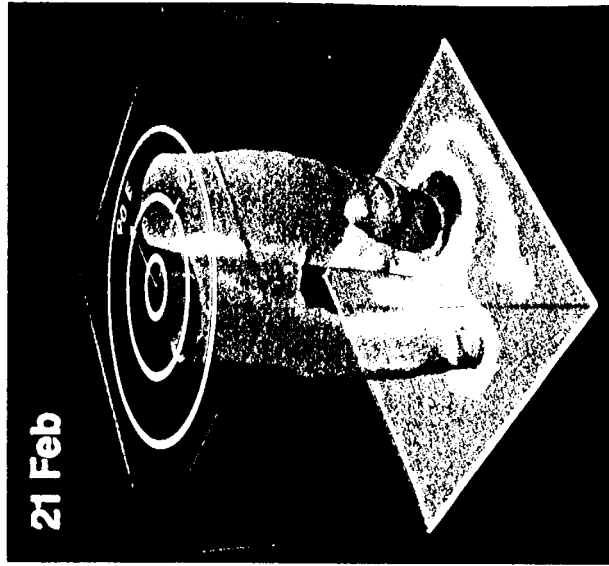
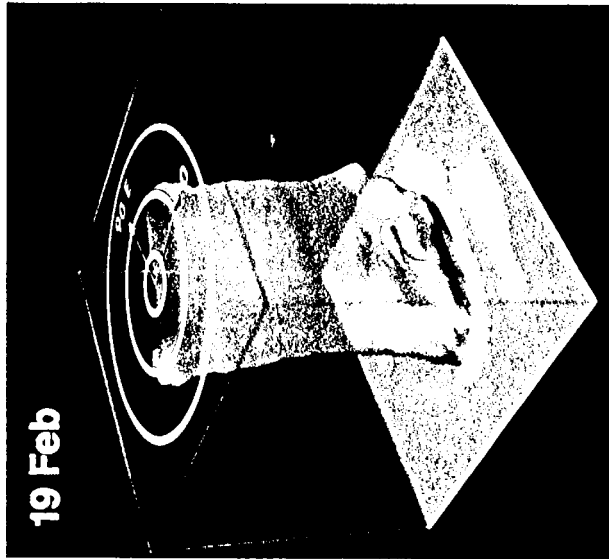
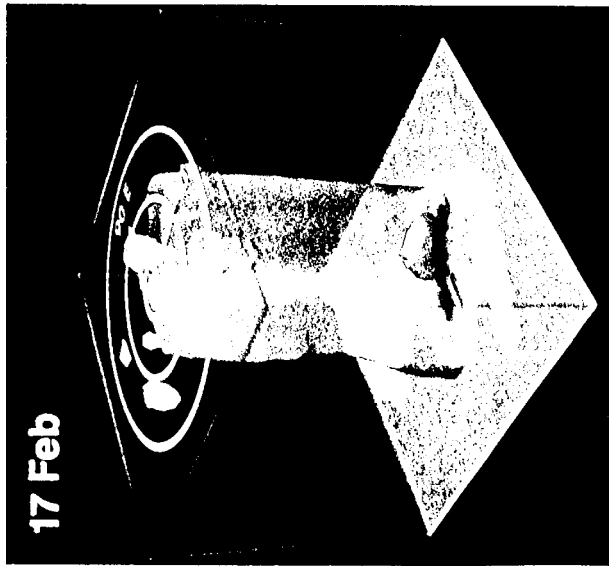
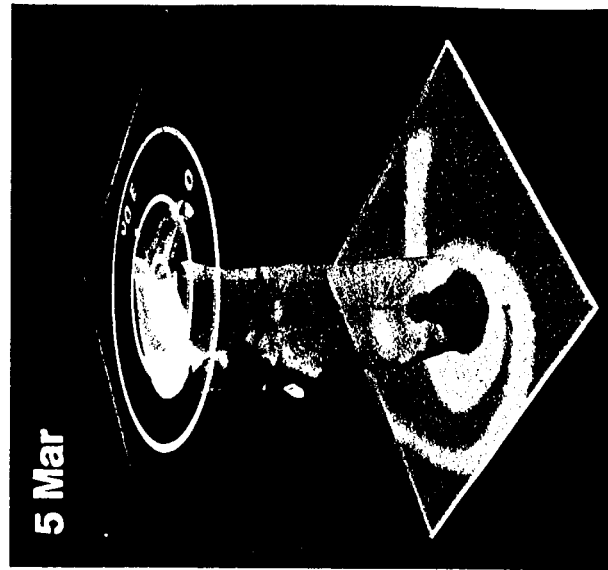
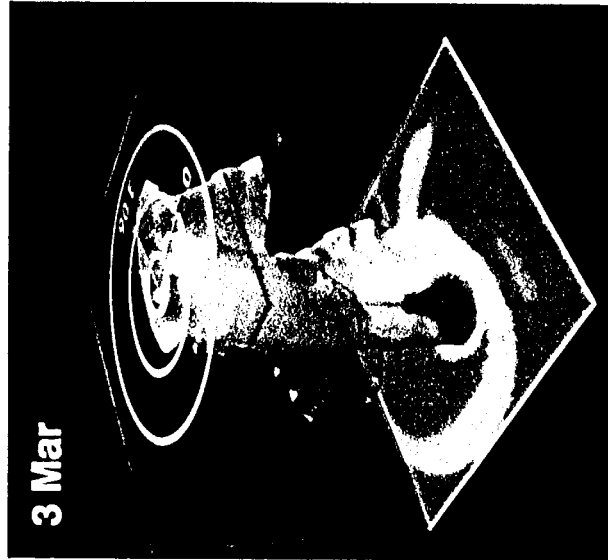
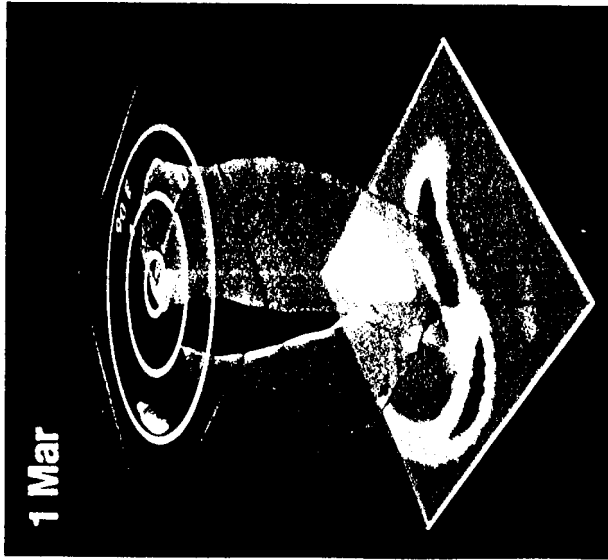


Fig. 13

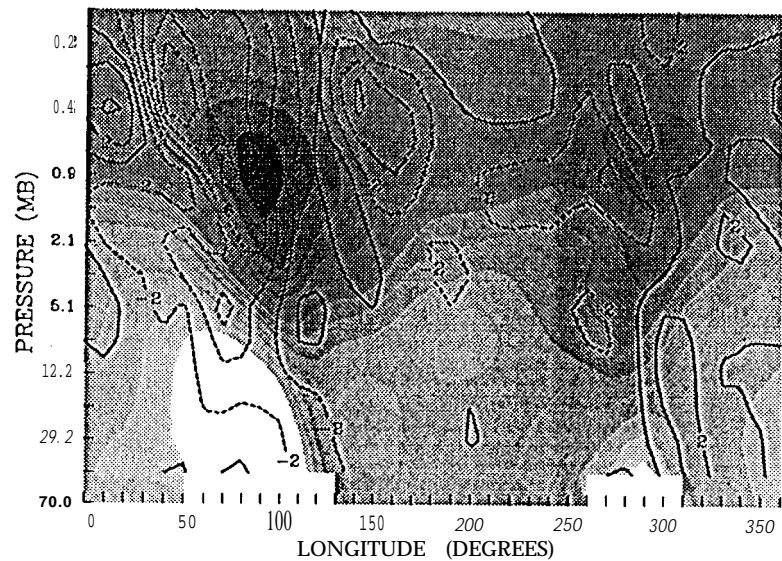
original in color



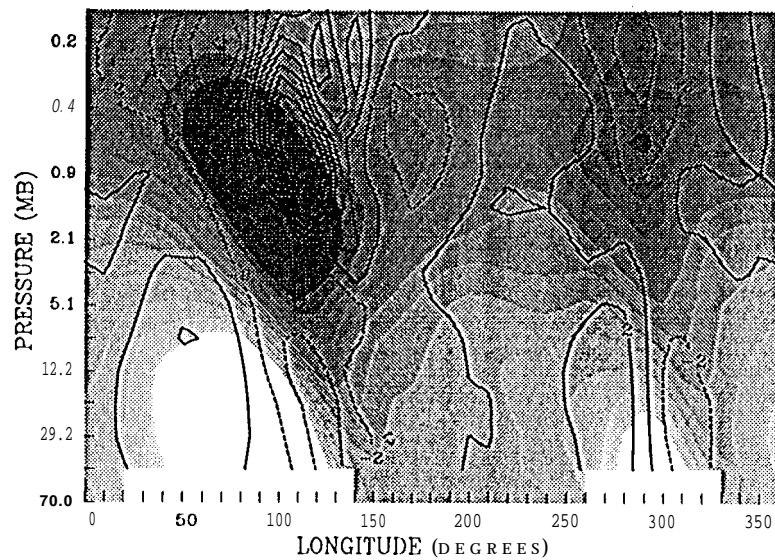
original in color



(a) ECM (LO) 60. DEG 19 FEB 1979



(b) ECM (LO) 60. DEG 21 FEB 1979

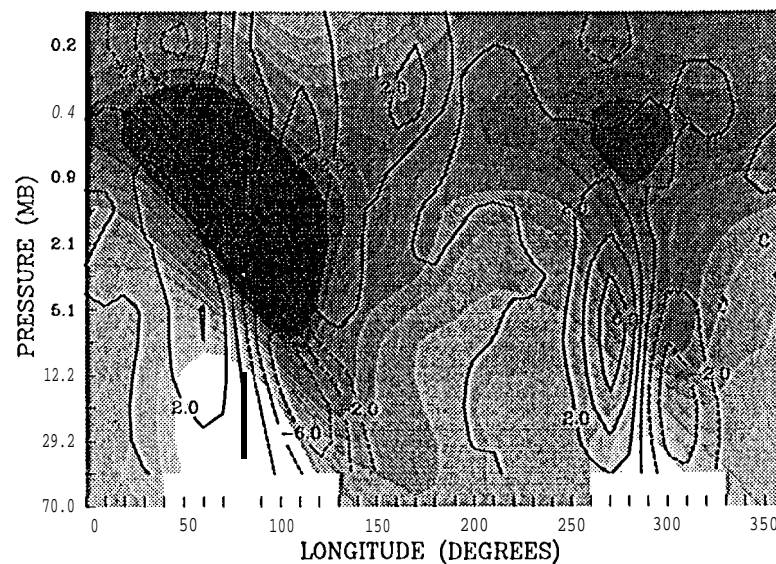


CoNTour FRom -2o TO 20 BY 2

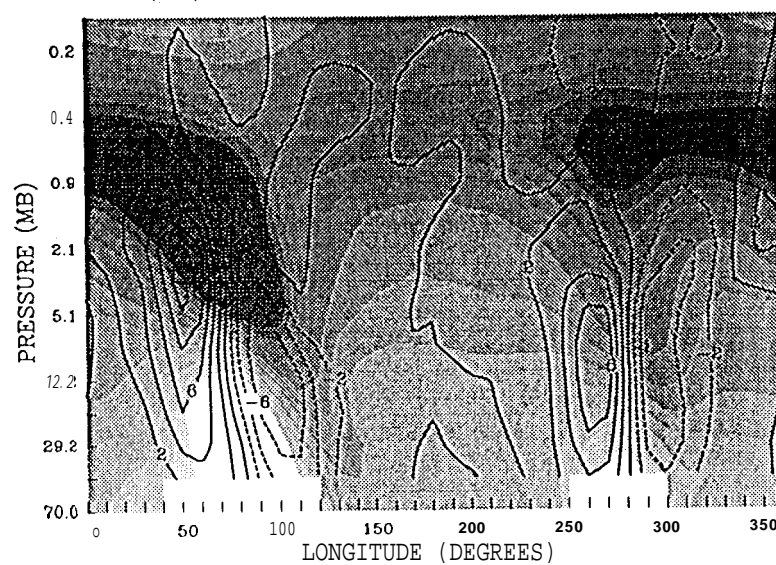


Fig. 15

(c) ECM (LO) 60. DEG 23 FEB 1979



(d) ECM (LO) 60. DEG 25 FEB 1979

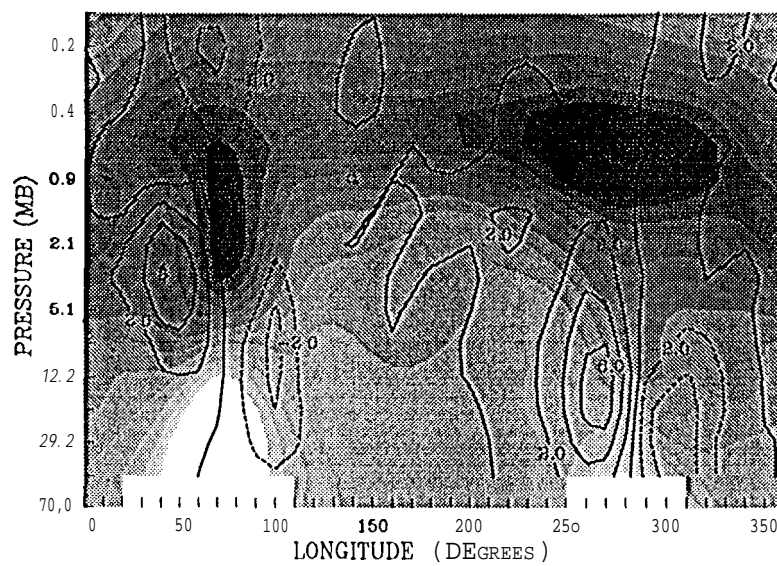


CONTOUR FROM -20 TO 20 BY 2



Fig. 15

(e) ECM (LO) 60. DEG 2'7 FEB 1979



CONTOUR FROM -20 TO 20 BY 2



Fig. 15

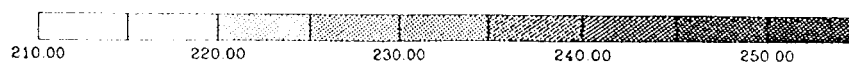
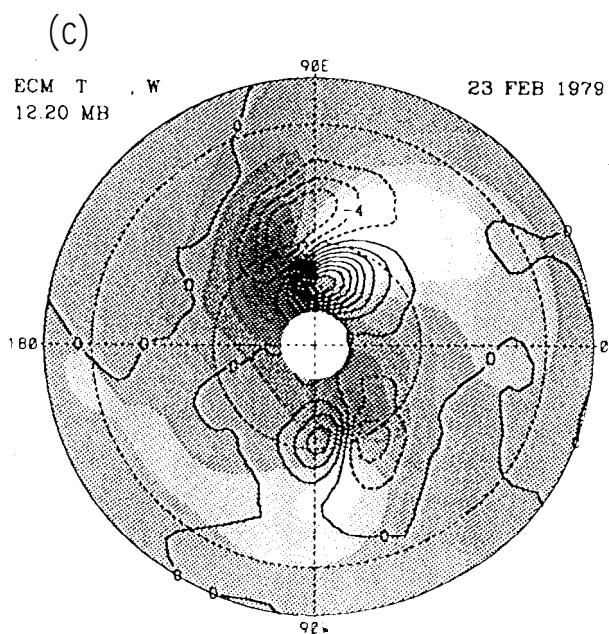
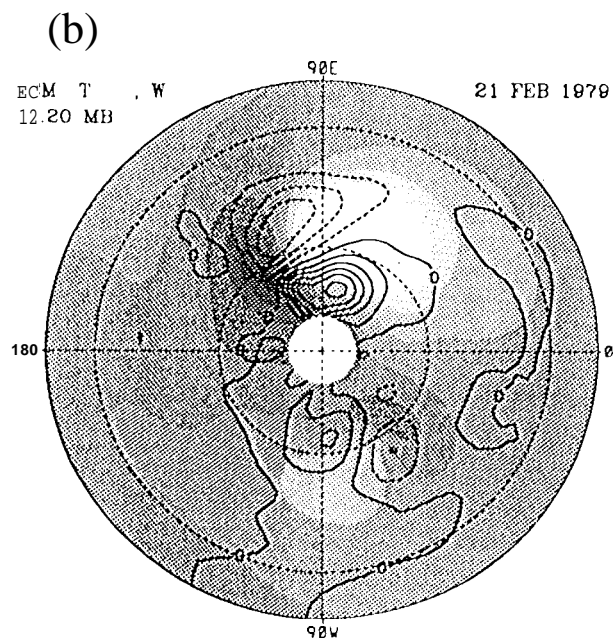
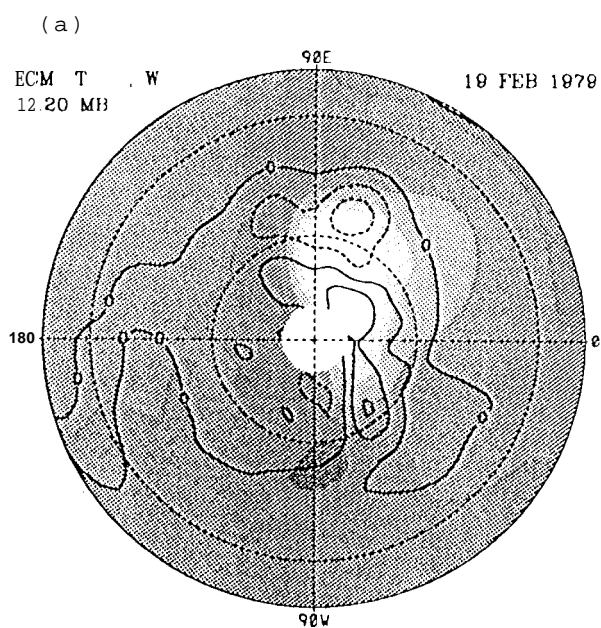
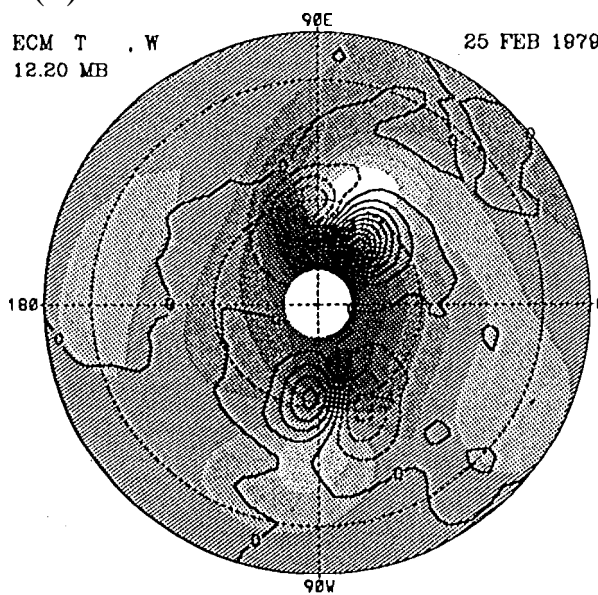


Fig. 16

(d)

ECM T . W
12.20 MB

25 FEB 1979



(e)

ECM T . W
12.20 MB

27 FEB 1979

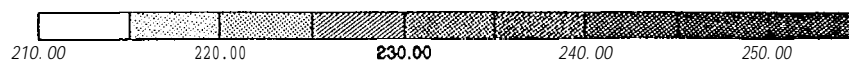
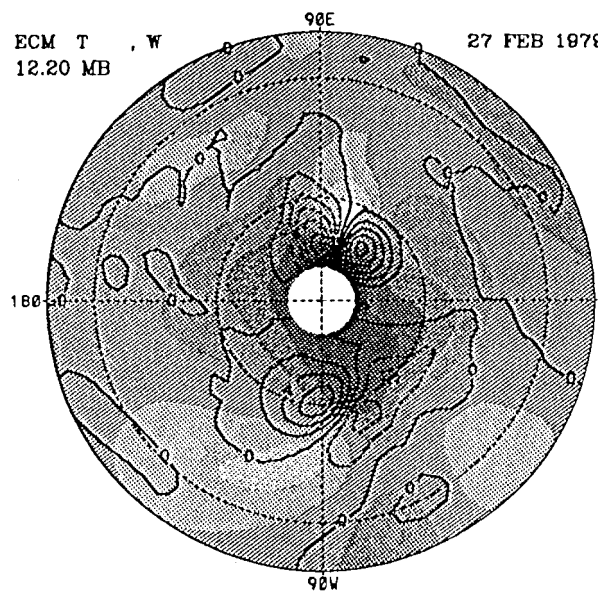


Fig. 16

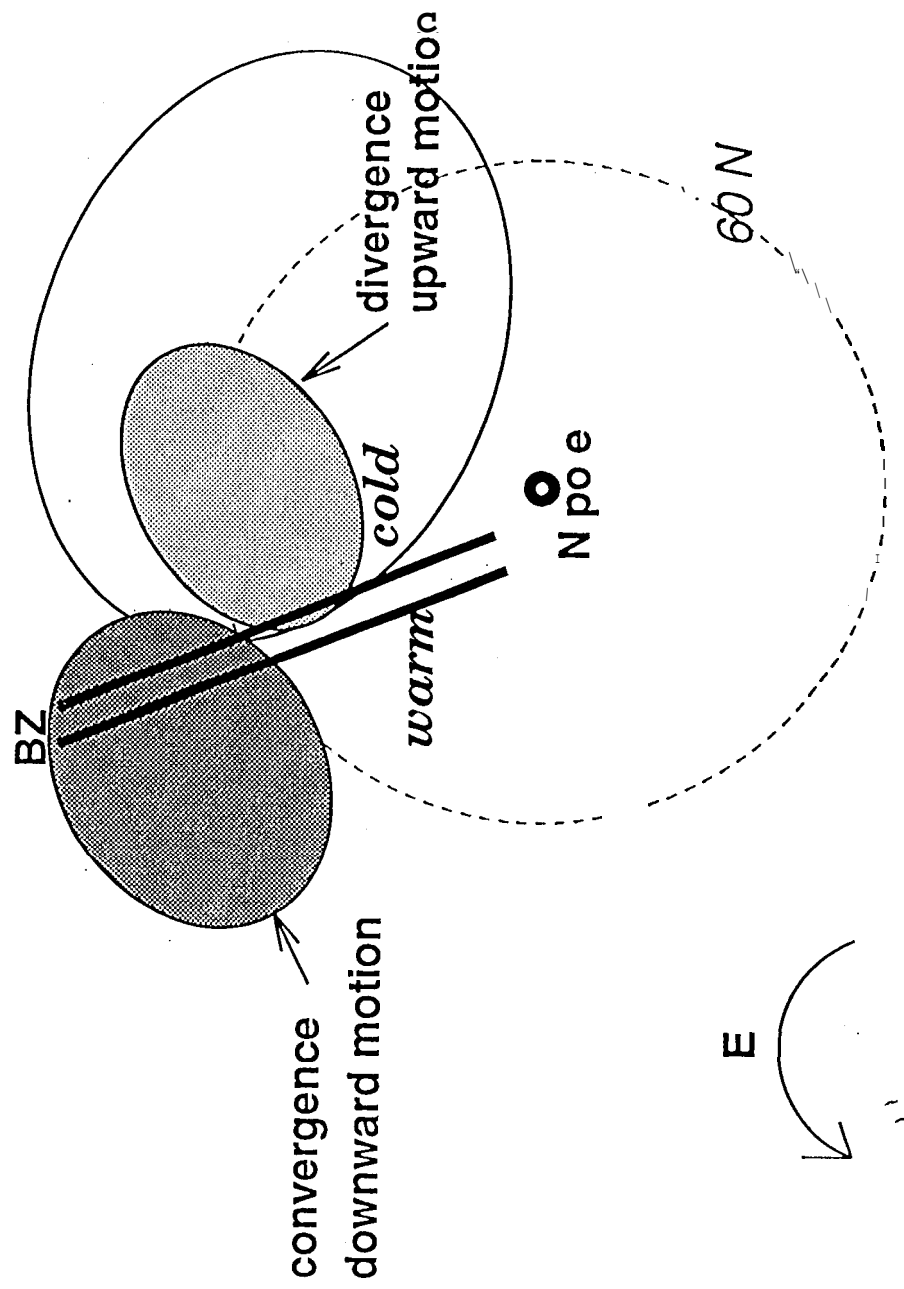


Fig. 17

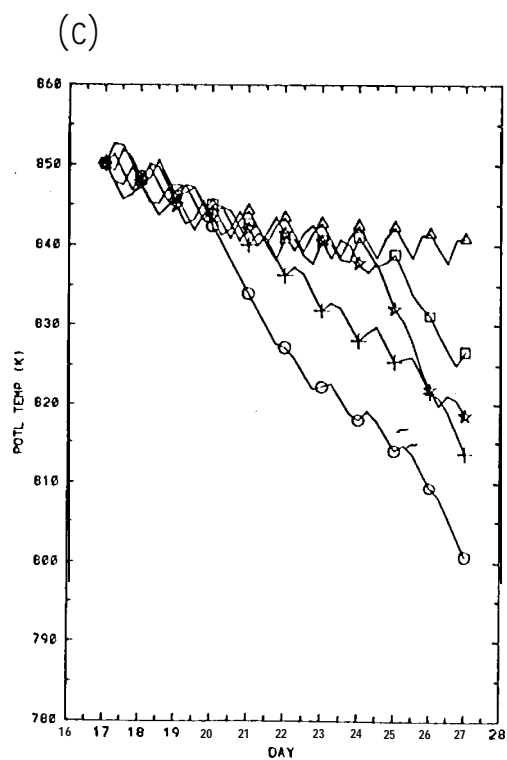
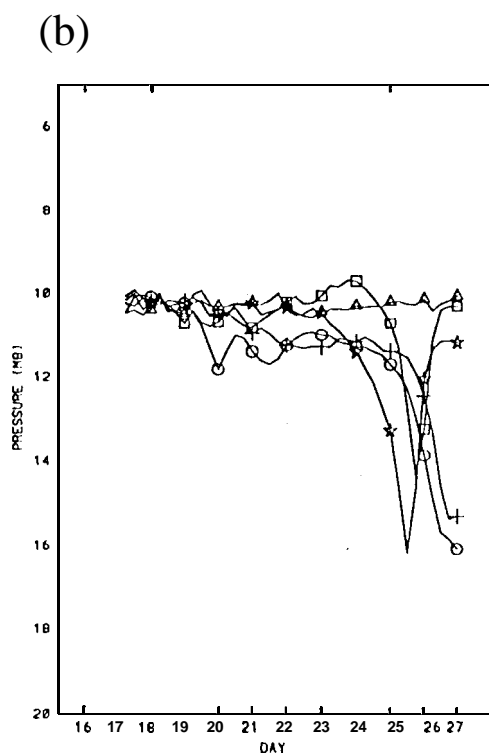
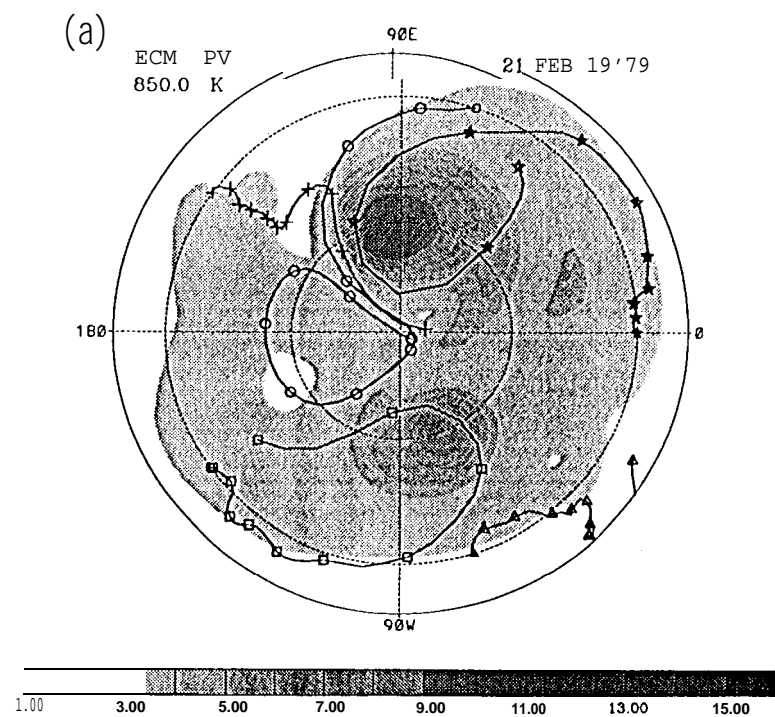


Fig. 18

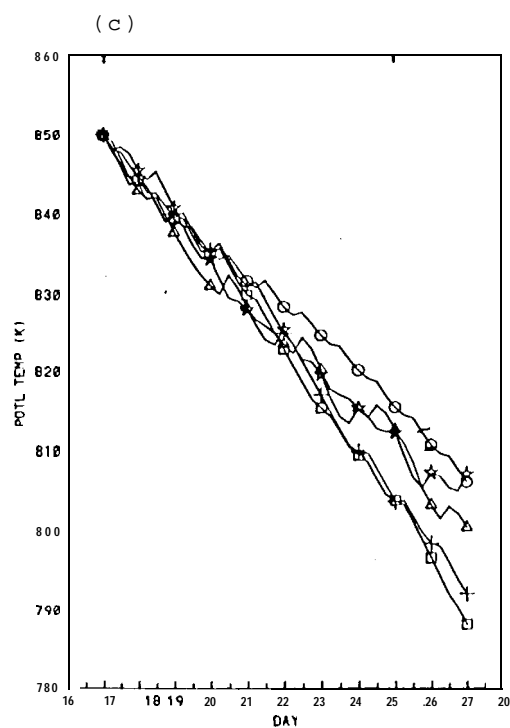
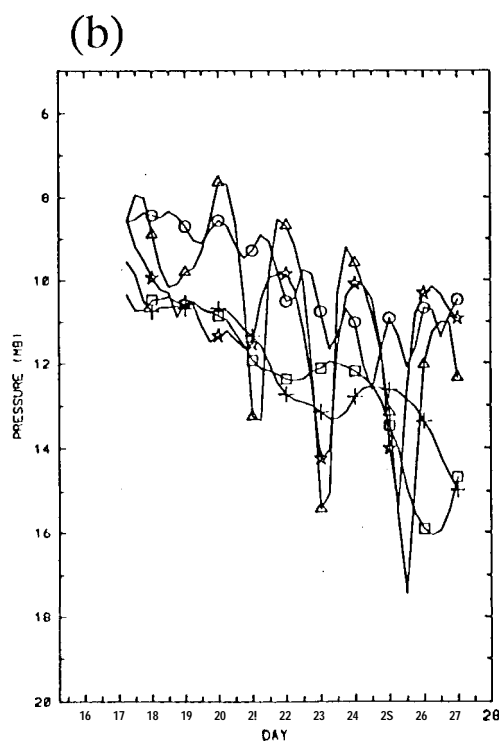
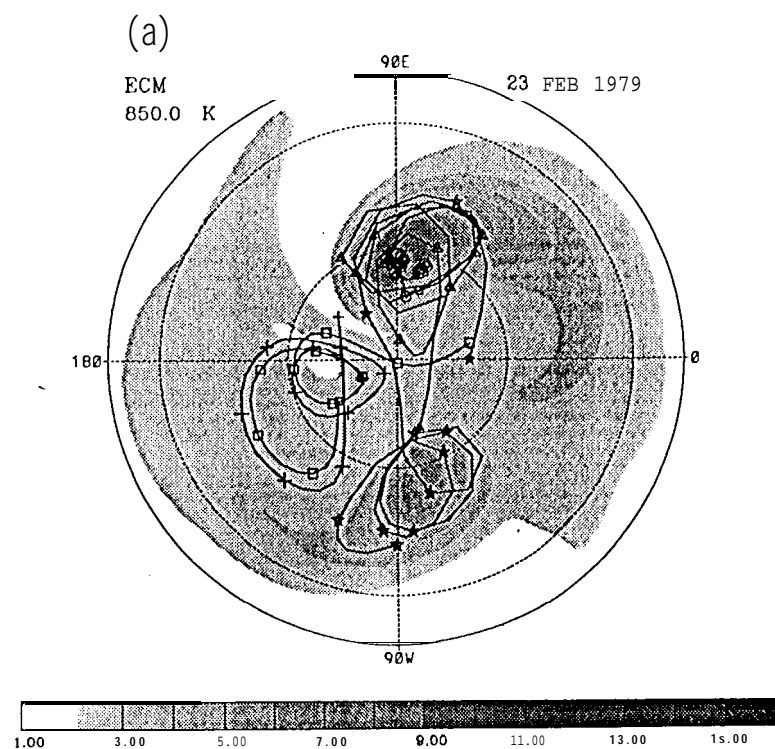


Fig. 19

ECM OZONE

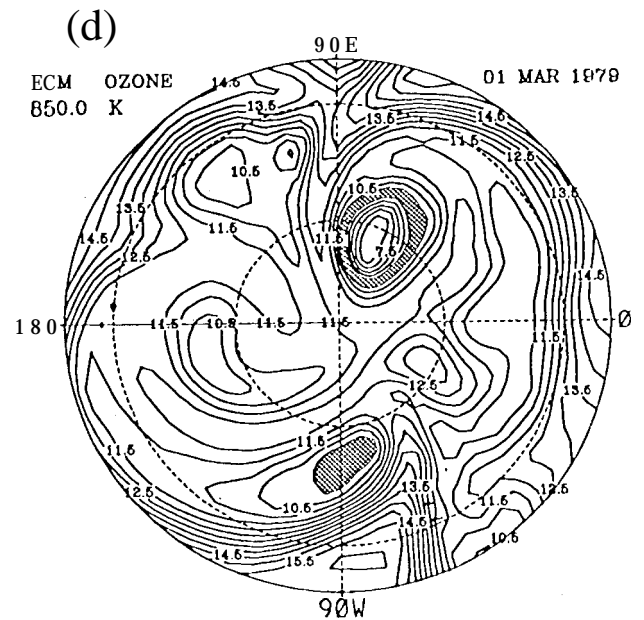
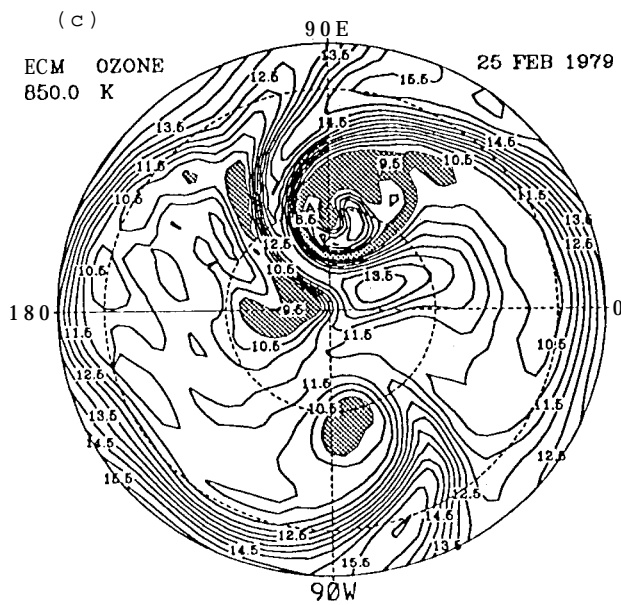
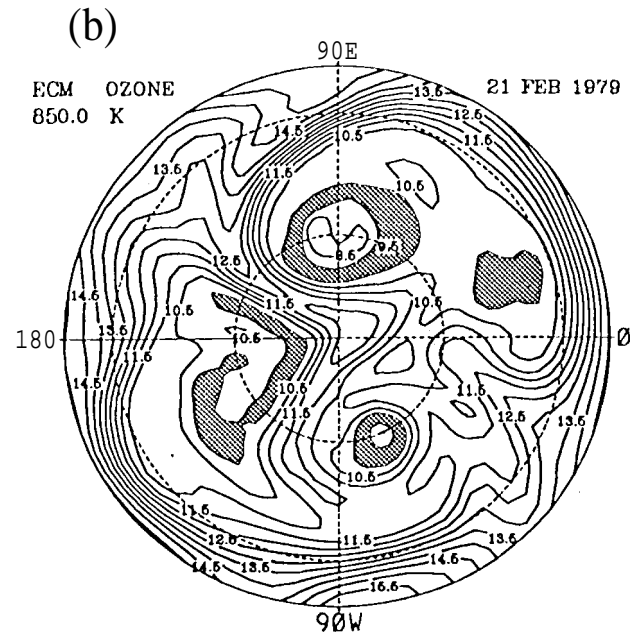
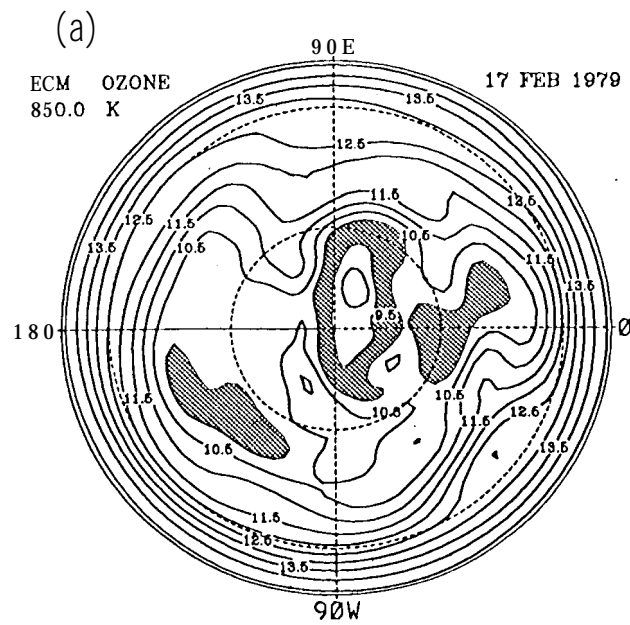
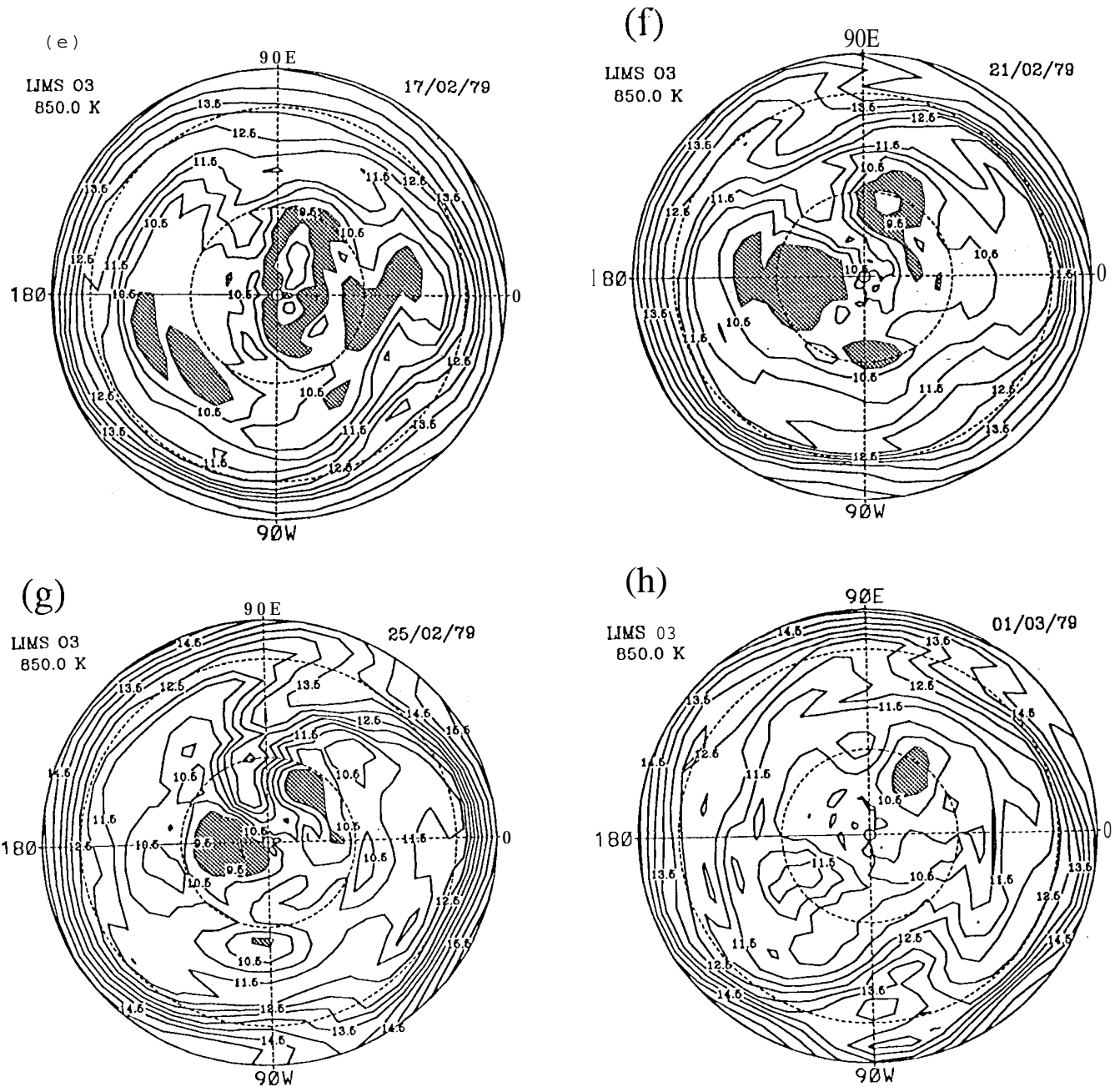
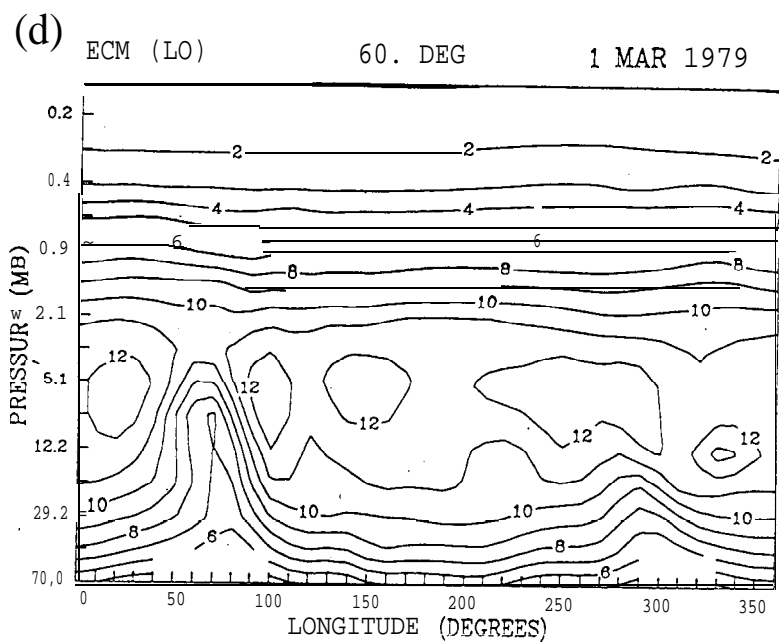
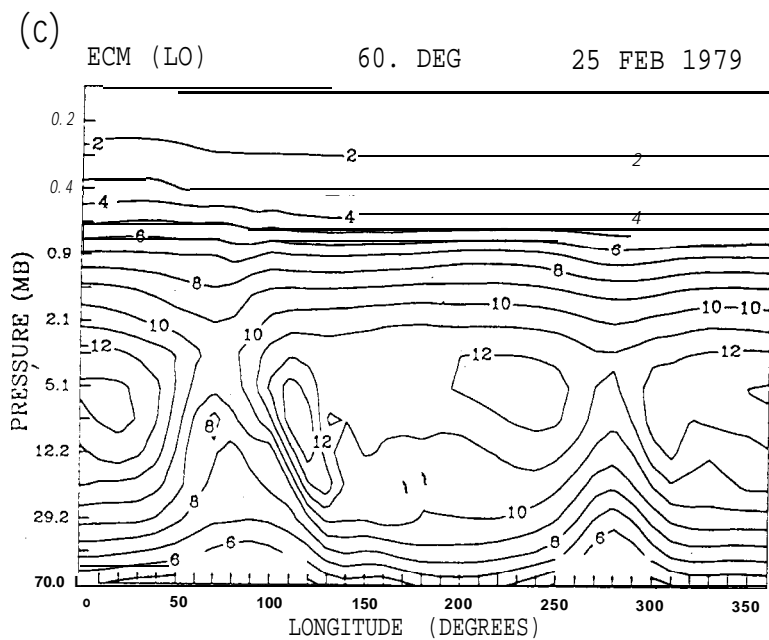
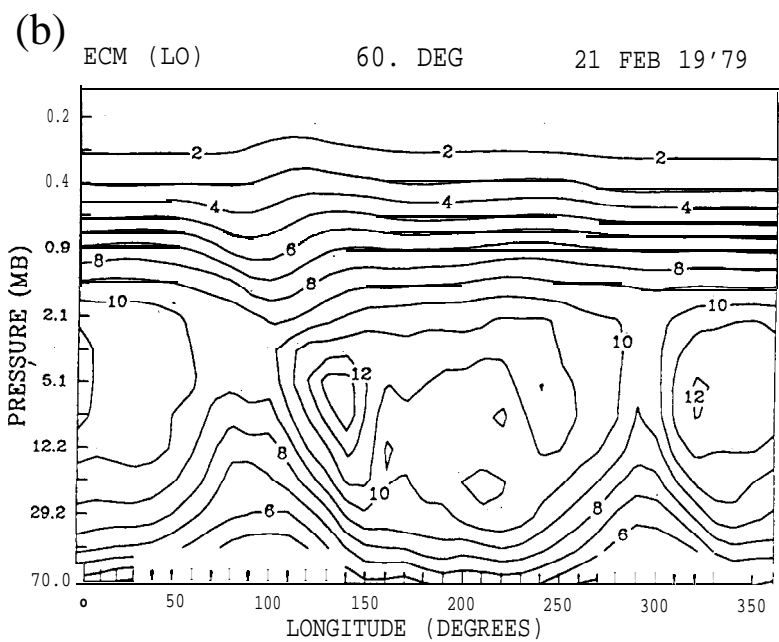
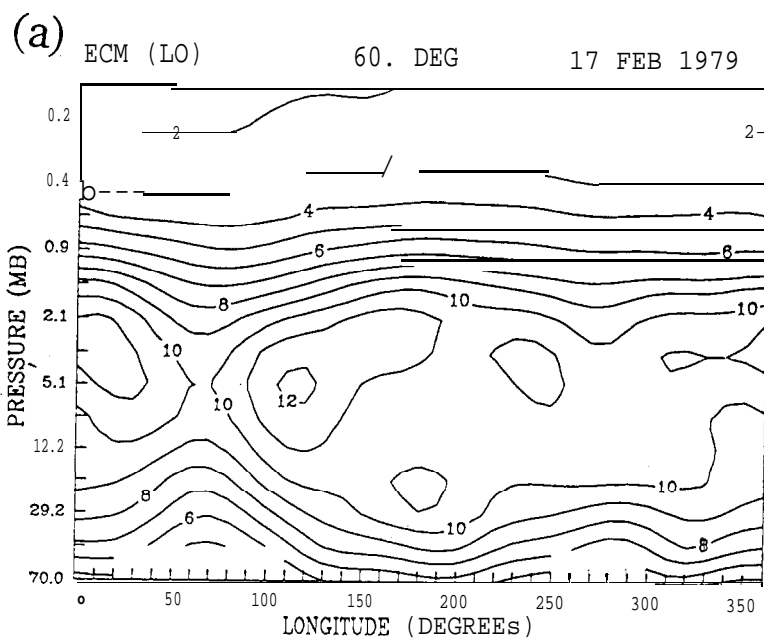
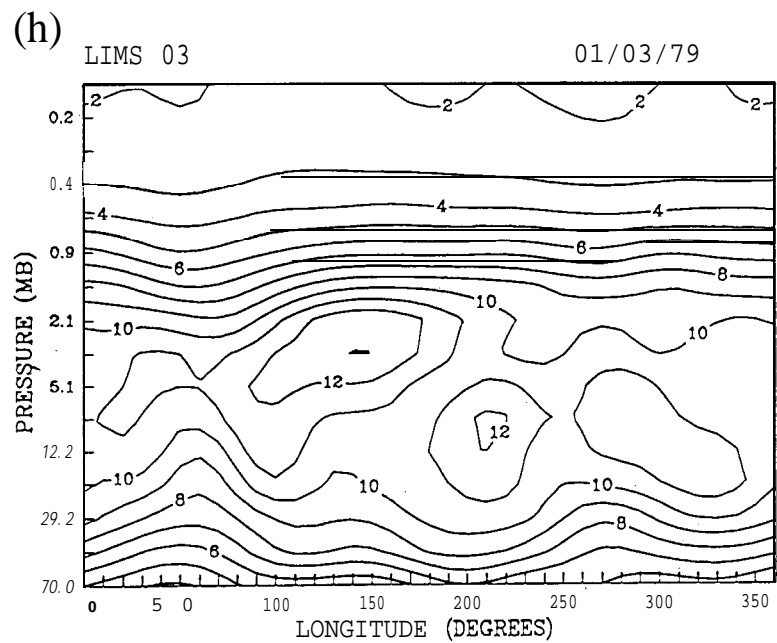
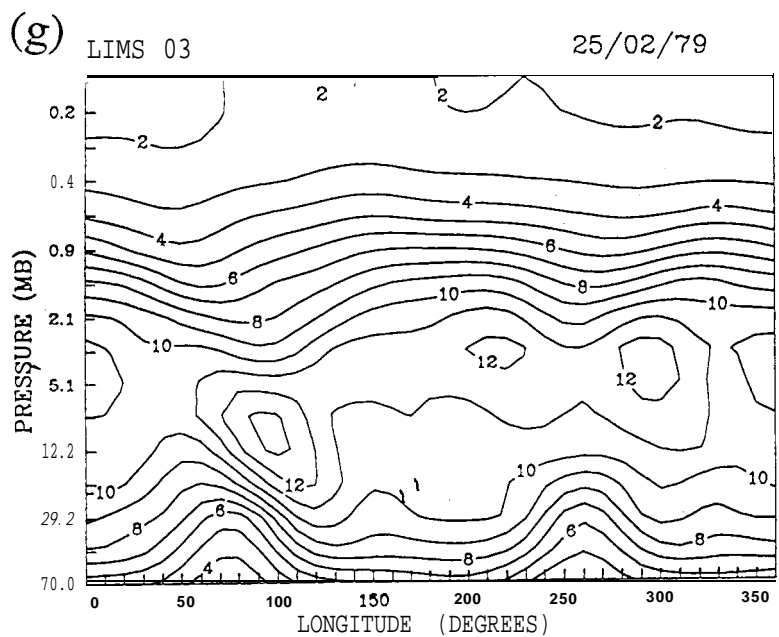
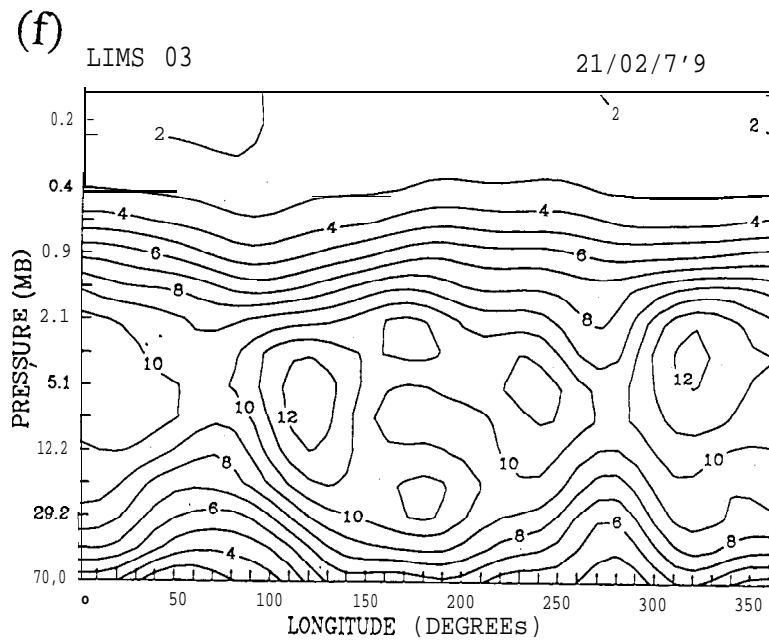
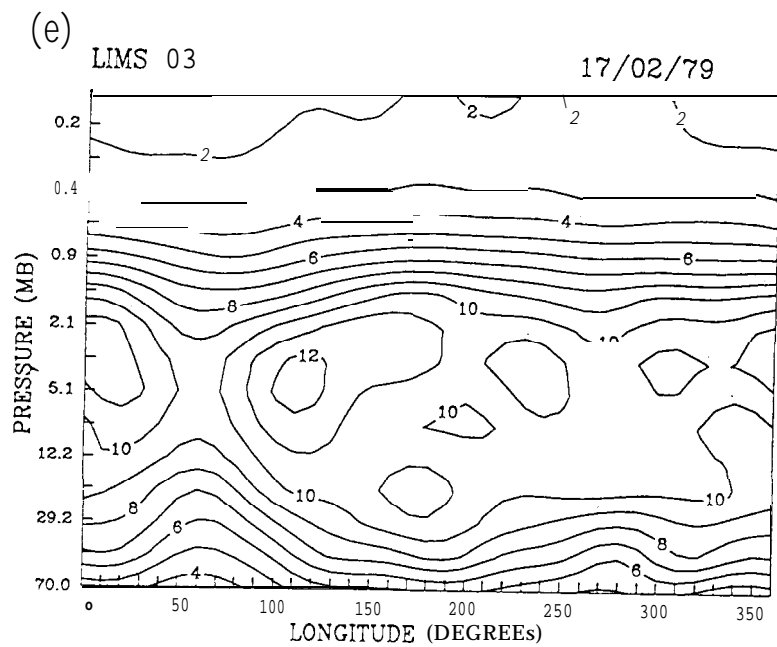


Fig. 20

LIMS OZONE

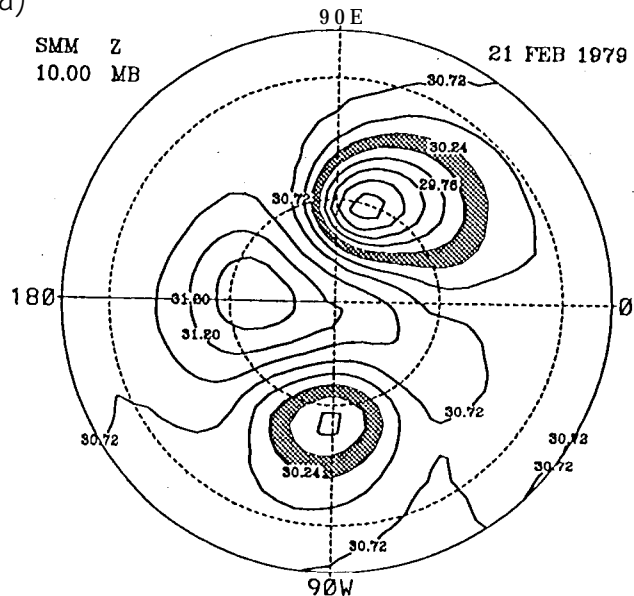






SMM HEIGHTS FGGE 15

(a)



(b)

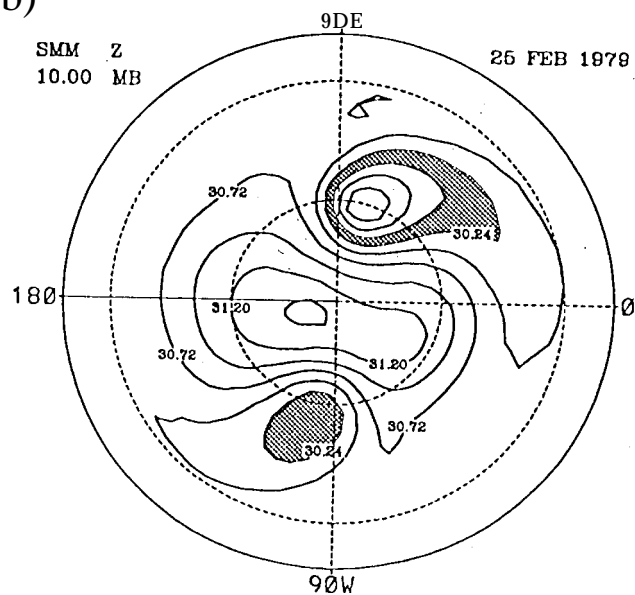


Fig. 23

